13 Boundary Layer Clouds

Clouds can form at the top of mixed layers, and at the bottom of stable boundary layers. The amount and distribution of short and long-wave radiative flux divergence in the boundary layer are altered by clouds, and these effects are emerging as important aspects of the climate-change problem. In addition, the radiative effects combine with latent heating to modulate BL dynamics, turbulence generation, and evolution. This chapter provides a brief review of cloud thermodynamics, radiative processes, the role of entrainment, and descriptions of fogs, cumulus and stratocumulus clouds.

13.1 Thermodynamics

13.1.1 Variables

Table 13-1 lists many of the thermodynamic variables that have been used in the literature to describe the state of the cloudy boundary layer. The ***static energies*** (s, s_v, s_e, s_L, s_{es}) are similar to the respective potential temperatures (θ, θ_v, θ_e, θ_L, θ_{es}). However, static energies are based on the assumption that any kinetic energy is locally dissipated into heat, while the potential temperatures do not utilize that assumption.

Static energies have units of m^2/s^2, or equivalently J/kg. Typical magnitudes for static energies in the boundary layer are 3×10^5 J/kg. By expressing static energies in units of kJ/kg, the resulting values are on the order of 300 kJ/kg. This helps to reinforce its analogy with potential temperature, which is typically on the order of 300 K.

Table 13-1. Thermodynamic variables useful for cloud studies. Many of the expressions are approximate.

Water Variables:

Mixing ratio (for water vapor)

r — $r = r_{sat}$ when the air is saturated

Saturated mixing ratio (for water vapor)

r_{sat} — calculated based on T and P

Liquid water mixing ratio

r_L

Total water mixing ratio

$r_T = r + r_L$

Temperature Variables:

Absolute temperature

T

Virtual temperature

$$T_v = T \cdot (1 + 0.61\, r - r_L)$$

Potential Temperature Variables:

Potential temperature

$$\theta = T \left(\frac{P_0}{P} \right)^{0.286} \cong T + \frac{g\, z}{C_p}$$

Virtual potential temperature

$$\theta_v = \theta \cdot (1 + 0.61\, r - r_L)$$

Equivalent potential temperature

$$\theta_e = \theta + \left(\frac{L_v\, \theta}{C_p\, T} \right) \cdot r$$

for unsaturated air, T is the parcel's temperature at the LCL

Liquid water potential temperature

$$\theta_L = \theta - \left(\frac{L_v\, \theta}{C_p\, T} \right) \cdot r_L$$

Saturation equivalent potential temperature

$$\theta_{es} = \theta + \left(\frac{L_v\, \theta}{C_p\, T} \right) \cdot r_{sat}$$

use calculated value of r_{sat} based on T and P

Static Energies:

Dry static energy (also known as the Montgomery stream function)

$$s = C_p T + g z$$

Virtual dry static energy

$$s_v = C_p T_v + g z$$

Moist static energy

$$s_e = C_p T + g z + L_v r$$

Liquid water static energy

$$s_L = C_p T + g z - L_v r_L$$

Saturation static energy

$$s_{es} = C_p T + g z + L_v r_{sat}$$ use r_{sat} calculated from T and P

Saturation Points:

Saturation point pressure

$$P_{SP}$$

Saturation point temperature

$$T_{SP}$$

Some of the characteristics of these variables are:

$s_L = s$	for unsaturated air
$s = s_{es}$	for saturated air
s_{es}	is conserved during ***moist*** adiabatic ascent/descent (no mixing)
s	is conserved during ***dry*** adiabatic ascent/descent (no mixing)
s_L and s_e	are conserved for both ***dry and moist*** adiabatic ascent/descent
$\partial s/\partial z$	determines ***dry static stability*** (stable if gradient is positive)
$\partial s_{es}/\partial z$	determines ***moist static stability*** (stable if gradient is positive)
r_T	is conserved for both ***dry and moist*** ascent/descent (no mixing and no precipitation).

Air is ***conditionally unstable*** if $\partial s/\partial z > 0$ and $\partial s_{es}/\partial z < 0$. Similar characteristics apply to the corresponding potential temperatures.

For air at a pressure level P, the ***saturation level*** is found by dry (moist) adiabatic ascent (descent) of an unsaturated air parcel (a saturated cloud parcel) to the pressure level, P_{SP}, where the parcel is just saturated with no cloud liquid water (Betts, 1982a&b, 1985). This level is also known as the ***lifting condensation level*** (LCL) for rising unsaturated air parcels, and often defines ***cloud base***. The temperature of an air parcel when moved to this level is symbolized as T_{SP}. On a thermodynamic diagram, the point represented by (P_{SP}, T_{SP}) is called the ***saturation point*** (SP).

13.1.2 Conserved Variables

Variables such as potential temperature and water-vapor mixing ratio are ***not conserved*** in a cloud, because of latent heat release/absorption and condensation/evaporation. We would rather use variables that are conserved under adiabatic processes regardless of the state of saturation of the air parcel, because then we can use those variables to study how diabatic processes and external forcings affect the evolution of the cloudy boundary layer.

The following variables ***are conserved*** for both dry and moist adiabatic processes with no precipitation, and change in proportion to the relative amounts of air undergoing isobaric mixing:

equivalent potential temperature,	θ_e
liquid-water potential temperature,	θ_L
moist static energy,	s_e
liquid water static energy,	s_L
total water mixing ratio,	r_T
saturation point pressure,	P_{SP}
saturation point temperature,	T_{SP}.

Any two of these conserved variables, together with the actual pressure or height of the air parcel, can be use to completely define the ***thermodynamic state and water content*** of the air (Betts and Albrecht, 1987). The most popular sets are (P, θ_e, r_T), (P, θ_L, r_T), (P, s_e, r_T), (P, s_L, r_T), or (P, P_{SP}, T_{SP}). Frequently, z is used in place of P in the above sets. Using any one set, we could calculate all of the variables listed in Table 13-1 (see Example 13.1.6).

By plotting one conserved variable against the other, we can create a ***conserved variable diagram*** that is useful for diagnostic studies of cloud and boundary layer processes (Hanson, 1984; Betts, 1985; Betts and Albrecht, 1987). Fig 13.1 shows a

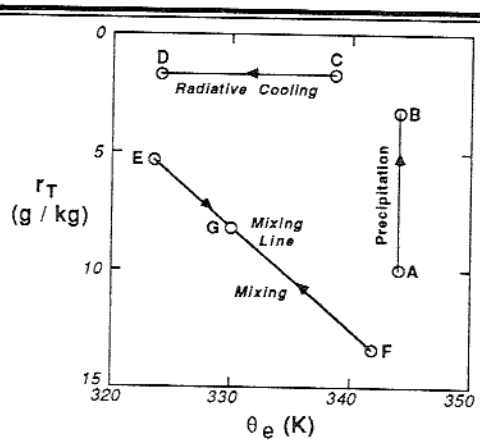

Fig. 13.1 Conserved quantity thermodynamic diagram (θ_e - r_T) showing how precipitation, radiation, and mixing affects the thermodynamic state of the air parcels labeled A through G. (After Betts, 1987).

θ_e - r_T diagram, along with some of the processes that can be represented. Precipitation leaving the parcel reduces r_T, but not θ_e. Radiative cooling affects θ_e, but not r_T. Mixing between two different air parcels results in a mixture parcel that falls on the ***mixing line***, a straight line connecting the thermodynamic states of the two original parcels. The portion of each original parcel in the final mixture is represented by the relative position along the mixing line.

Fig 13.2 shows a θ_e - r_T diagram for data from the CCOPE experiment in Montana. It is clear that a deep layer between about 85 kPa (850 mb) and almost 60 kPa (600 mb) is undergoing mixing, because the data falls along a mixing line. This mixing includes both the subcloud boundary layer and the vigorous cumulus convection above. At cloud top levels (60 to 50 kPa) radiative cooling dominates.

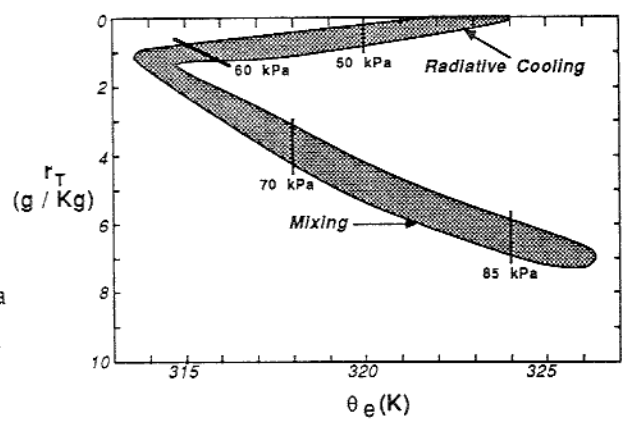

Fig. 13.2 Conserved parameter diagram for two soundings on 6 August 1981, during CCOPE, showing lower troposphere mixing line structure. The 85, 70, 60, and 50 kPa p-level altitudes are also indicated. (After Betts, 1985).

13.1.3 Conservation Equations for Turbulent Flow

Conservation of total water (3.4.4b) has already been discussed in Chapter 3. It is rewritten here in terms of a total water mixing ratio, and molecular diffusion is neglected:

$$\frac{\partial \overline{r_T}}{\partial t} + \overline{U_j}\frac{\partial \overline{r_T}}{\partial x_j} = \frac{S_{rT}}{\overline{\rho}_{air}} - \frac{\partial \overline{u_j' r_T'}}{\partial x_j} \qquad (13.1.3a)$$

where S_{rT} is a body source term that is negative for net precipitation leaving the air parcel, and is positive for net precipitation falling into the parcel. Change of water phase within the parcel does not alter the total water conservation.

Conservation of heat is rewritten in terms of s_L, although s_e or the corresponding potential temperatures can be used instead:

$$\frac{\partial \overline{s_L}}{\partial t} + \overline{U}_j \frac{\partial \overline{s_L}}{\partial x_j} = -\frac{1}{\overline{\rho} C_p} \frac{\partial \overline{Q_j^*}}{\partial x_j} - \frac{\partial \overline{u_j' s_L}}{\partial x_j} \qquad (13.1.3b)$$

where molecular conduction has been neglected. The evaporation term in (3.4.5b) does not appear because phase change is already incorporated into the definition of the liquid water static energy.

The fluxes at the top of a ML are found using the entrainment parameterizations:

$$\overline{w' r_T'}_{z_i} = -w_e \Delta_{EZ} \overline{r_T} \qquad (13.1.3c)$$

$$\overline{w' s_L'}_{z_i} = -w_e \Delta_{EZ} \overline{s_L} \qquad (13.1.3d)$$

where $\Delta_{EZ}( )$ is the usual jump across the top of the ML. Rogers, et al. (1985a) suggest the following parameterization for fluxes at the surface (in this case, over an ocean):

$$\overline{w' r_T'}_s = C_E \overline{M} [r_{sat}(T_s) - r_T] \qquad (13.1.3e)$$

$$\overline{w' s_L'}_s = C_H \overline{M} [s_s - \overline{s_L}] \qquad (13.1.3f)$$

The buoyancy flux is needed to calculate TKE production, entrainment production vs. consumption, or to find scaling variables such as w_*. Moeng and Randall (1984) suggest that:

$$\overline{w' s_v'} = \alpha_1 \overline{w' s_L'} + \alpha_2 \overline{w' r_T'} \qquad (13.1.3g)$$

where $\alpha_1 = 1$ and $\alpha_2 = 0$ for unsaturated air. For cloudy air:

$$\alpha_1 = \alpha_3 \left[1 + 1.61\, T \frac{\partial r_{sat}}{\partial T} \right]$$

$$\alpha_2 = \alpha_3 \left[L_v \left(1 + 0.61\, T \frac{\partial r_{sat}}{\partial T} \right) \right]$$

$$\alpha_3 = \left[1 + \frac{L_v}{C_p} \frac{\partial r_{sat}}{\partial T} + 1.61\, T \frac{\partial r_{sat}}{\partial T} \right]^{-1}$$

Buoyancy variables such as s_v can be computed (using iteration) from the variables listed in Table 13-1 (see Example 13.1.6).

13.1.4 Saturation Point and the Lifting Condensation Level

To use many of the variables in Table 13-1 for a saturated air parcel, we must be able to determine the saturation mixing ratio. Empirical fits to the saturation curve have been reviewed by Buck (1981), Bolton (1980), Lowe (1977), Wexler (1976), and Stackpole (1967). Bolton suggests that a variation of ***Tetens' formula*** (1930) is sufficiently accurate to determine the saturation (with respect to liquid) water-vapor pressure (in units of kPa) for typical BL temperatures:

$$e_{sat} = (0.61078\ \text{kPa}) \cdot \exp\left[\frac{17.2694 \cdot (T - 273.16)}{T - 35.86} \right] \qquad (13.1.4a)$$

for absolute temperature in (K).

The saturation mixing ratio is then found from:

$$r_{sat} = 0.622 \frac{e_{sat}}{P - e_{sat}} \qquad (13.1.4b)$$

for pressure P in the same units as e_{sat}. Sometimes the variation of saturation mixing ratio with temperature is needed. The ***Clausius-Clapeyron equation*** can be written as:

$$T \frac{dr_{sat}}{dT} = 0.622 \frac{L_v\, r_{sat}}{\Re\, T} \qquad (13.1.4c)$$

The ***saturation point*** (SP) temperature and pressure are found from the following approximation:

$$T_{SP} = T_{LCL} = \frac{2840}{3.5 \ln(T) - \ln\left(\frac{P \cdot r}{0.622 + r} \right) - 7.108} + 55. \qquad (13.1.4d)$$

and

$$P_{SP} = P_{LCL} = P \cdot \left(\frac{T_{SP}}{T} \right)^{3.5} \qquad (13.1.4e)$$

for P in kPa and T in K (Bolton, 1980; Wilde, et al., 1985). The lifting condensation level is the saturation level for an unsaturated parcel lifted dry adiabatically. As was shown in Chapter 11, many convective thermals have undiluted cores, allowing the actual ***cloud base*** to be very close to the LCL calculated from surface-layer air.

13.1.5 Convection and Cloud Available Potential Energies

Not all clouds are positively buoyant. The buoyancy of a rising air parcel can be written as: $g \cdot (\Delta\theta_v / \theta_v)$, or approximately as $g \cdot (\Delta s_v / s_v)$, where $\Delta\theta_v = \theta_{v\ \text{cloud}} - \theta_{v\ \text{environ.}}$

and $\Delta s_v = s_{v\,cloud} - s_{v\,environ.}$. Fig 13.3 shows four key levels of a convective cloud:

- cloud base (near the LCL)
- level of free convection (LFC)
- limit of convection (LOC)
- cloud top

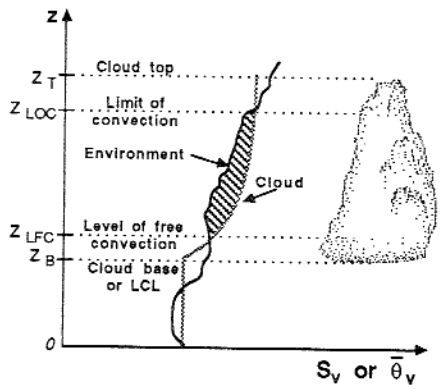

Fig. 13.3 Four key levels in an active cloud are related to condensation and buoyancy. The convective available potential energy (CAPE) is proportional to the shaded area.

Although condensation starts to occur in the parcel at ***cloud base***, this condensation often forms in the negatively buoyant overshoot of a ML thermal into its capping inversion. Latent heat is released as the parcel rises. If the parcel has sufficient inertia to overshoot high enough, its potential temperature might rise to the point where it is again warmer than the environment. This point, where the cloudy parcel is first positively buoyant, is called the ***level of free convection*** (LFC). A cloud that reaches its LFC is classified as an ***active cloud***.

The cloud parcel continues to rise due to its own buoyancy while $\Delta\theta_v$ or Δs_v is positive. The cloud temperature can be estimated by following a moist adiabat. Eventually, the rising parcel reaches a level where it is cooler than the environment. This point is called the ***limit of convection***. The cloud parcel might overshoot beyond the limit of convection because of its inertia, eventually stopping its overshoot at ***cloud top***.

A variety of available potential energies can be defined from cloud properties. The vertical integral of the parcel buoyancy between the LFC and LOC defines the ***convective available potential energy*** (CAPE):

$$\text{CAPE} = \int_{z=z_{LFC}}^{z_{LOC}} \frac{g}{\theta}\,\Delta\theta_v(z)\,dz \qquad (13.1.5a)$$

and is indicated as the shaded area in Fig 13.3. A velocity scale, w_{CAPE}, can be defined

by assuming that all the potential energy is converted into kinetic energy (Rogers, et al., 1985):

$$w_{CAPE} = (2 \cdot CAPE)^{1/2} \qquad (13.1.5b)$$

This scale can be used to model the overshoot of the cloud top above the LOC.

The ***evaporative available potential energy*** (EAPE) can be defined similarly as (13.1.5a), except for the negative buoyancy associated with the evaporation of liquid water within a sinking cloudy parcel (Betts, 1985). This can be used to study cloud-top entrainment.

13.1.6 Example

Problem: Assume that the following measurements of (p, s_L, r_T) were obtained in a cloud and the surrounding environment, respectively: (80 kPa, 304.1 kJ/kg, 16.5 $g/kg)_{cloud}$ and (80 kPa, 307.0 kJ/kg, 10 $g/kg)_{env}$. Is the cloudy parcel positively or negatively buoyant?

Solution: To determine buoyancy, we must calculate s_v for both the cloud and environment. First, we can use the equations in Table 13-1 to write the expression for s_v:

$$s_v = C_p T \cdot [\, 1 + 0.61r - r_L \,] + g z \qquad (13.1.6a)$$

Next, we can use the ***hypsometric equation*** to find gz:

$$\begin{aligned} g z &= \Re \overline{T_v} \ln(p_o/p) \\ &= \Re \overline{T} \ln(p_o/p) \cdot [\, 1 + 0.61r - r_L \,] \end{aligned} \qquad (13.1.6b)$$

where the overbar represents an average over the layer between p_o and p. Since we have no information about the temperature between those two levels, we will use the local value of T and r_T at p for simplicity. We will assume a reference level of $z = 0$ at $p_o = 100$ kPa.

Environment: In the unsaturated environment, $r_L = 0$ and $r = r_T$. Thus:

$$s_L = s = C_p T + g z \qquad (13.1.6c)$$

Combining this with the previous equation gives:

$$g z = \frac{s_L}{1 + \left[\frac{\Re}{C_p} \cdot \ln\left(\frac{p_o}{p} \right) \cdot (1 + 0.61\, r_T) \right]^{-1}} \qquad (13.1.6d)$$

Using $\Re/C_p = 0.286$, $p_o/p = 100/80$, and $r_T = 0.01$ g/g, the term in square brackets becomes 0.0642. This yields $g\,z = 18{,}523\ m^2 s^{-2}$.

Combining (13.1.6a) and (13.1.6c) yields an expression for the environmental virtual static energy in terms of the knowns: s_L, r_T, and $g\,z$:

$$\begin{aligned} s_v &= s_L + 0.61\, r_T\, (s_L - gz) \\ &= 307000 + (0.61)\cdot(0.01)\cdot(307000 - 18523) \\ &= 308760\ \text{J/kg} \\ &= 308.8\ \text{kJ/kg} \end{aligned}$$

Cloud: In a saturated environment: $r_T = r_{sat} + r_L$. Thus, the liquid water static energy becomes:

$$s_L = C_p\, T + g\, z - L_v\, r_T + L_v\, r_{sat} \qquad (13.1.6e)$$

If we assume for simplicity that $gz_{cloud} = gz_{environ.}$, then all of the terms in the above equation are known except T and r_{sat}. But since r_{sat} is a function of T (and p) via Teten's formula, we can iteratively solve for the temperature that satisfies (13.1.6e). The solution is T = 289.25 K and $r_{sat} = 14.54$ g/kg.

The virtual static energy in the cloud is thus:

$$\begin{aligned} s_v &= C_p\, T \cdot [\, 1 + 1.61\, r_{sat} - r_T\,] + g\, z \\ &= (1004)\cdot(289.25)\cdot[\, 1 + (1.61)\cdot(0.01454) - 0.0165\,] + 18523 \\ &= 310937\ \text{J/kg} \\ &= 310.9\ \text{kJ/kg} \end{aligned}$$

Buoyancy: The cloud is more buoyant than the environment, because $s_{v\ cloud} > s_{v\ environ}$.

Discussion: We could have made the problem much simpler by defining our coordinate system such that z = 0 at p = 80 kPa. Since both the cloudy and environmental air parcels are at the same height for this problem, the gz terms would have disappeared. Although this approach is acceptable for determining relative buoyancy, the magnitudes of the resulting virtual static energies would differ from those usually obtained with a reference height of 100 kPa.

Although it was stated earlier that any two of the conserved variables plus the pressure or height are sufficient to solve for any other conserved variable, we see in this example that the solution can be far from trivial. The problem lies in the nonlinear dependency of

saturation mixing ratio on temperature. Computerized solutions can be designed to iterate the equations to solve for temperature. Alternately, linearized simplifications can be used (Betts, 1982) to give an approximate solution.

13.2 Radiation

The physics relevant for radiation within and between clouds requires knowledge of liquid water content, cloud droplet size distribution, cloud temperature, cloud surface shape, cloud cover, solar zenith angle, and many more (Welch and Wielicki, 1984; Schmetz and Beniston, 1986). It is a very complex problem that is beyond the scope of this book. We will focus on only the simplest parameterizations here for continuous stratus/stratocumulus cloud decks. By neclecting radiation from cloud sides and weighting the radiation budget by the cloud cover, the stratocumulus radiation parameterization below can be extended in crude form to scattered cumulus clouds.

Fig 13.4 shows profiles of upward and downward short and longwave radiation for a stratocumulus-topped marine boundary layer during the day (Nicholls, 1984). Solar radiation is absorbed over a depth on the order of hundreds of meters in the top of this cloud, while infrared radiative divergence occurs within about 30 m of the cloud top and bottom. These are discussed in more detail next.

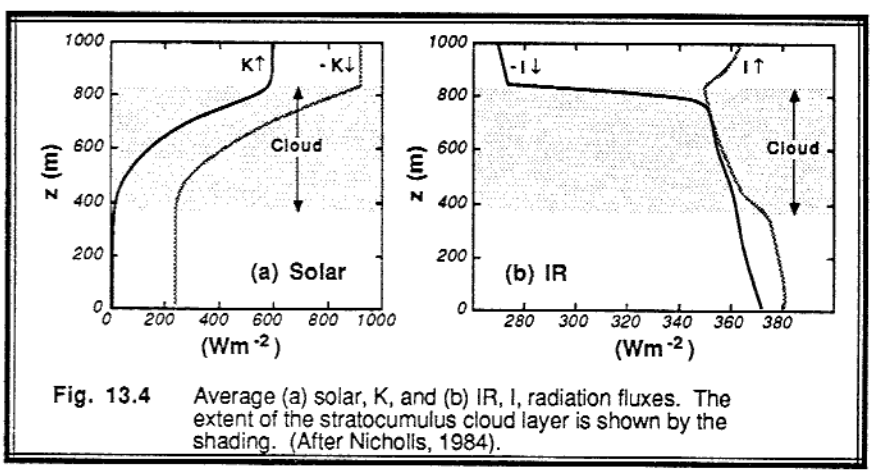

Fig. 13.4 Average (a) solar, K, and (b) IR, I, radiation fluxes. The extent of the stratocumulus cloud layer is shown by the shading. (After Nicholls, 1984).

13.2.1 Solar

Fig 13.5 shows the vertical profile of net solar radiation ($K^* = K\downarrow + K\uparrow$) for an idealized 500 m thick cloud within a 1000 m thick BL (Hanson, 1987). The exponential decrease in net radiation with depth below cloud top causes warming within the top 100 to 200 m of the cloud. Lower in the cloud there is less absorption and less heating. There is no noticeable solar flux divergence at cloud base. The cloud shades the ground, reducing

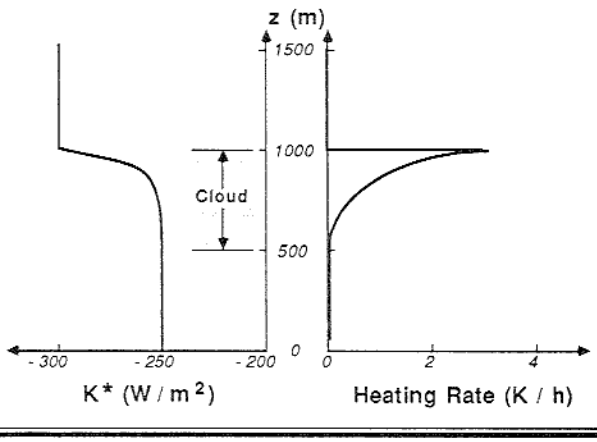

Fig. 13.5 Profiles of net shortwave radiative flux and the corresponding heating rate in an idealized stratocumulus deck. (After Hanson, 1987).

the surface heating and the associated convection during the daylight hours.

Hanson and Derr (1987) have proposed the following simplified parameterization for solar radiation absorption. It is assumed that the heights of cloud top and base are known (z_T and z_B, respectively).

$$K^*(z) = K_T^* - (K_T^* - K_B^*) \cdot \frac{1 - \exp\left[\frac{-(z_T - z)}{\lambda_{sol}}\right]}{1 - \exp\left[\frac{-(z_T - z_B)}{\lambda_{sol}}\right]} \qquad (13.2.1a)$$

where the e-folding solar decay length, λ_{sol}, is approximated by:

$$\lambda_{sol} \cong 15 \cdot W_p^{0.335} \qquad (13.2.1b)$$

The decay length is typically in the range of 50 to 150 m. The liquid water path, W_p, is:

$$W_p \equiv \int_{z_B}^{z_T} \rho_{air}\, r_L\, dz$$

$$\cong \frac{(z_T - z_B)^2}{880} \qquad (13.2.1c)$$

where the last approximation gives W_p in units of g/m^2, for cloud heights in units of m. The liquid water mixing ratio is assumed to increase linearly with height from cloud base to cloud top, associated with moist adiabatic ascent. This latter assumption appears

realistic for the midlatitude marine stratocumulus studied by Nicholls and Leighton (1986), but less realistic for the arctic stratus clouds studied by Curry (1986). Typical liquid water paths vary between about 10 and 1000 g/m^2. Fravalo, et al. (1981) find that the flux profiles are particularly sensitive to the liquid water content distribution.

The bulk cloud albedo, a_c, and absorption, b_c, are used to find the net shortwave fluxes at the top and bottom of the cloud (K_T^* and K_B^*, respectively, positive for upward flux):

$$K_T^* = (1 - a_c)\, K\downarrow$$
$$K_B^* = (1 - a_c - b_c)\, K\downarrow \qquad (13.2.1d)$$

The second equation above describes the transmission of downward solar radiation through the cloud. The downward solar flux at the top of the cloud deck, $K\downarrow$, is always negative, and can be found from (7.3.1b). The albedo and absorption are a function of the liquid water path and the solar zenith angle, as shown in Fig 13.6 (Stephens, 1978). Stephens also presents a parameterization for these curves. One must be careful using either the figures or the parameterization to ensure that the sum of the albedo and absorption do not exceed one (a problem for large liquid water paths and small zenith angles).

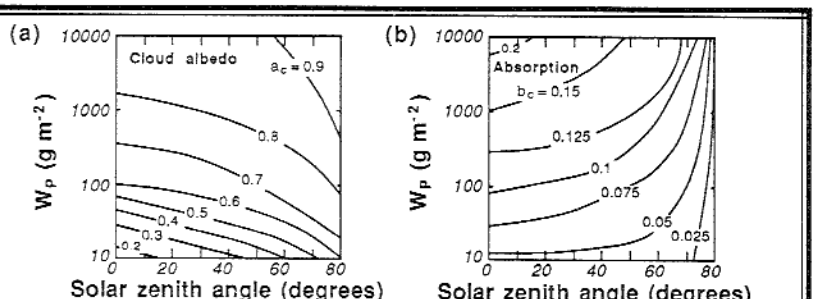

Fig. 13.6 The variability of (a) cloud albedo and (b) shortwave absorption as determined by a theoretical model for changes of solar incidence and liquid water path (W_P). The surface albedo is zero and a tropical moisture profile is assumed. The contours are the fraction of the incident downward flux at the cloud-top reflected or absorbed. (After Stephens, 1978).

13.2.2 Infrared

Fig 13.7 shows an example of the longwave radiative flux profile through a stratocumulus deck, and the associated heating rate. Water droplets are such efficient absorbers/emitters of IR radiation that the cloud essentially behaves as a black body. The changes in radiative flux associated with the cloud occur with an e-folding length of only about 30 m, causing a sharp cooling spike at cloud top and heating spike at cloud base.

Although there is some debate as to exactly where these heating and cooling spikes actually occur, we will assume that they occur just within the cloud boundaries.

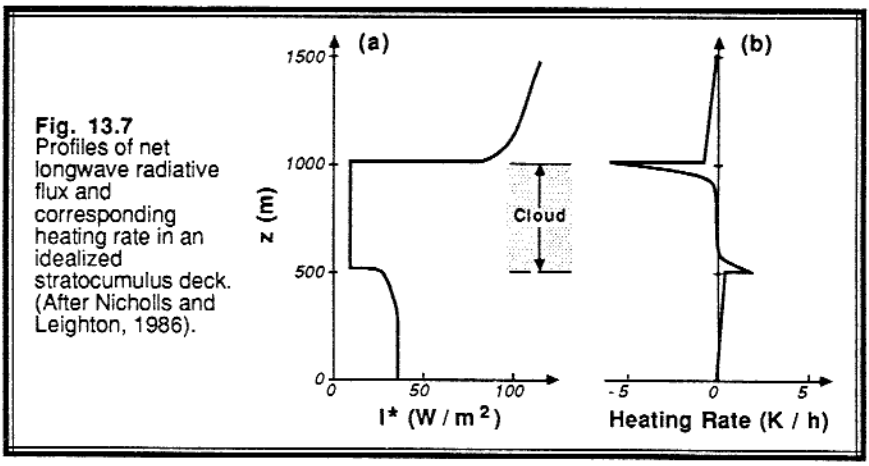

Fig. 13.7 Profiles of net longwave radiative flux and corresponding heating rate in an idealized stratocumulus deck. (After Nicholls and Leighton, 1986).

If fine resolution modeling of the flux divergence is required, a parameterization such as proposed by Hanson and Derr (1987) and Hanson (1987) could be used. Otherwise, a simpler approach allows all of the flux divergence to occur across a small fixed distance such as 30 m. Rogers, et al. (1985a) modeled the change in net longwave flux across the top (ΔI^*_T) and bottom (ΔI^*_B) of the cloud as:

$$\Delta I^*_T = \frac{\sigma_{SB}}{\rho\, C_p}\left(T^4_{\text{cloud top}} - T^4_{\text{sky}} \right) \qquad (13.2.2a)$$

$$\Delta I^*_B = \frac{\sigma_{SB}}{\rho\, C_p}\left(T^4_{\text{surface}} - T^4_{\text{cloud base}} \right) \qquad (13.2.2b)$$

where ($I^* = I\downarrow + I\uparrow$) is the net longwave radiation, positive upward.

13.3 Cloud Entrainment Mechanisms

13.3.1 Cloud-top Entrainment Instability in Stratocumulus

Lilly (1968) first suggested that the warm air entrained into the top of a stratocumulus cloud might cool and sink if it were initially dry enough to support considerable evaporative cooling of the neighboring cloud droplets. His criterion for this unstable entrainment state was $\Delta_{EZ}\theta_e < 0$, for $\Delta_{EZ}\theta_e = \theta_{e\ \text{just above cloud top}} - \theta_{e\ \text{just below cloud top}}$. Randall (1980) and Deardorff (1980) recognized that the virtual potential temperature was a better measure of buoyancy and instability, and suggested a minor modification to Lilly's criterion:

Entrainment is unstable if: $\Delta_{EZ}\theta_e < \Delta_{EZ}\theta_{e\ critical}$ (13.3.1a)

where the critical equivalent potential temperature jump across cloud top is (Rogers, et al., 1985a):

$$\Delta_{EZ}\theta_{e\ critical} = \frac{\theta \cdot \Delta_{EZ} r_T}{\alpha_4} \tag{13.3.1b}$$

The factor α_4 is:

$$\alpha_4 = \frac{1 + 0.609\, r_{sat} + 1.609\left(T\frac{dr_{sat}}{dT}\right)}{1 + \frac{L_v}{C_p T}\left(T\frac{dr_{sat}}{dT}\right)} \tag{13.3.1c}$$

Negatively buoyant downdrafts formed from the entrained air produce additional TKE that can enhance mixing and entrainment. The newly entrained air can then also become unstable and sink, resulting in even more TKE and more entrainment. This positive feedback process can cause a cloud to entrain large amounts of dry air, resulting in the rapid breakup and evaporation of the cloud.

A number of investigators have suggested that (13.3.1a) is a necessary but not sufficient condition for unstable entrainment (Hanson, 1984). Rogers and Telford (1986) learned that some additional trigger or initial disturbance is required to start the whole process. Albrecht, et al. (1985) pointed out that even if the criteria above are satisfied, the cloud might not break up if the mixture between the entrained and cloudy air is unsaturated.

13.3.2 Entrainment into Cumulus

Although lateral entrainment might be the dominant mixing mechanism for unsaturated thermals, it appears to play a minor role for many of the cumulus clouds studied. Entrainment through the top of the cloud is more important. In this process, entrained air at cloud top partially mixes with some of the cloudy air, and the mixture cools because of the evaporation of some of the cloud droplets, just like stratocumulus cloud-top entrainment instability. The result is a negatively buoyant downdraft (see Fig 13.8) that sinks through the cloud and mixes with other cloudy air along the way (Pontikis, et al., 1987).

Although Squires (1958) had originally proposed this mechanism, it wasn't until the mixing analysis by Paluch (1979) that the ***cloud top entrainment*** mechanism was confirmed and better understood. Her analysis, modified here using the techniques of Betts (1985), uses conserved variables to diagnose the origins of air measured at various levels within a cloud.

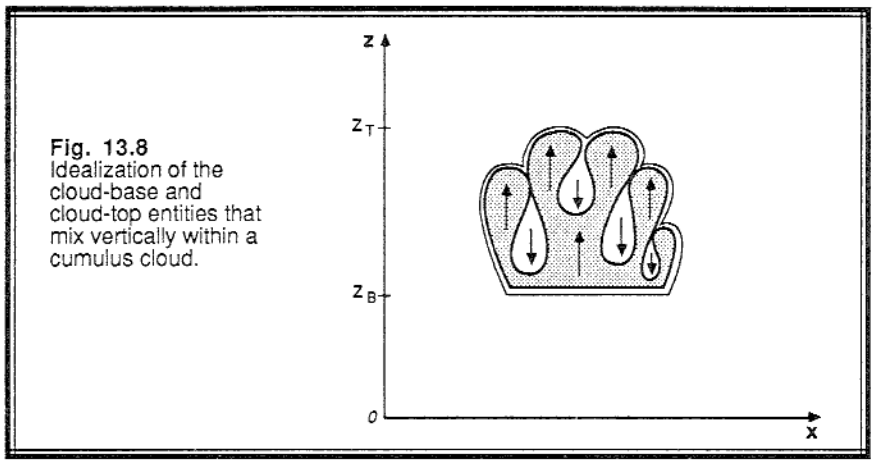

Fig. 13.8 Idealization of the cloud-base and cloud-top entities that mix vertically within a cumulus cloud.

Fig 13.9 shows an idealized conserved variable plot of an environmental sounding. Measurements within clouds, plotted as the data points in Fig 13.9, lie on, or close to, a straight line connecting a point on the environmental sounding corresponding to cloud-base or subcloud layer air, and another point on the environmental sounding at the height of cloud top. The fact that most of the measurements fall on the same straight ***mixing line*** indicates that air originating from cloud base and cloud top are mixed together in various proportions and left within the cloud.

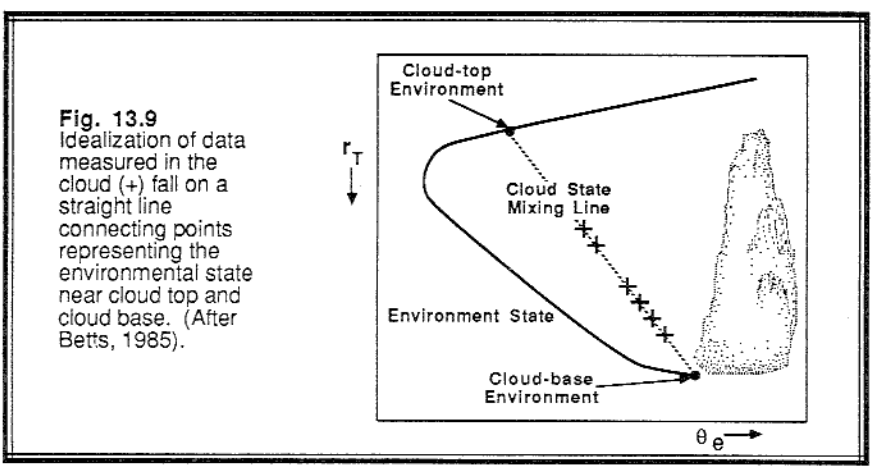

Fig. 13.9 Idealization of data measured in the cloud (+) fall on a straight line connecting points representing the environmental state near cloud top and cloud base. (After Betts, 1985).

If environmental air from other levels between cloud base and cloud top were entrained into the cloud, then data points would lie between the environmental line and the mixing line drawn in Fig 13.9. Since few such data points are usually observed, we must conclude that most of the air within the cloud came from cloud base and cloud top (Blyth

and Latham, 1985; Jensen, et al., 1985). A further indication of the importance of cloud-top entrainment is that the spread of cloud droplet sizes is smaller than would be observed if lateral entrainment was a more prominent process. (Raymond and Blyth, 1986; Kitchen and Caughey, 1981).

Many of Telford's observations show a bimodal or multimodal droplet size distribution that further supports the cloud top entrainment mechanism (Rogers, et al., 1985b). This prompted him to propose an ***entity-type entrainment mixing*** model (Telford and Chai, 1980; Telford, et al., 1984), where there are various different but individually well-mixed entities or blobs that move to their respective levels of neutral buoyancy, and which together form the cloud as sketched in Fig 13.8. Raymond and Blyth (1986) extended this approach to allow a variety of mixing proportions between cloud top and cloud base air.

Betts (1986) and Betts and Miller (1986) have used mixing line results to develop a convective adjustment parameterization for use in large-scale models. Betts and Albrecht (1987) further noted that evaporation of falling precipitation into parts of the cloud can cause penetrative downdrafts that result in kinks in the mixing line.

In addition to thermodynamic mixing-line analyses of mixing, there have been a variety of direct observations of eddy motion fields. Kitchen and Caughey's (1981) tethered-balloon observations showed a circulation pattern shaped like a "?" or a backwards "P" (see Fig 13.10). Eymard (1984) observed a greater vertical velocity variance immediately under clouds than at the same altitude between clouds. Brümmer and Wendel (1987) confirmed that there are often downdrafts along and just outside of the lateral edges of cumulus clouds. Stith, et al. (1986) found that the updrafts at middle levels in the cloud have diameters smaller than the cloud, but that near cloud top the updraft is more diffuse and wider, implying significant mixing at cloud top.

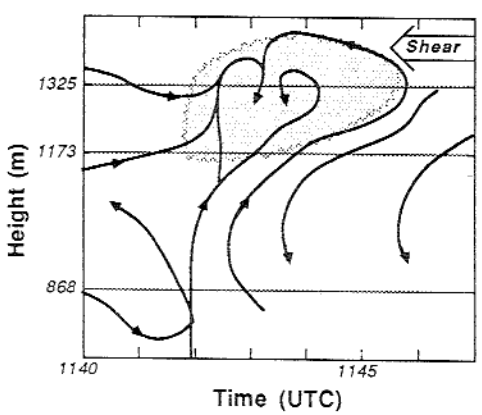

Fig. 13.10
Flow vectors constructed from the u,v, and w wind components near a cloud (shaded). A suggested flow pattern, marked with heavy lines, has an inclined updraft overturning at cloud top in the direction of the mean wind shear. This circulation assumes the shape of a "?". (After Kitchen and Caughey, 1981).

13.4 Fair-weather Cumulus

13.4.1 Cloud Classification

Fair-weather cumulus clouds can be divided into three classes based on their dynamics (see Fig 13.11): ***forced, active***, and ***passive*** (Stull, 1985). This classification is different than the morphological categorization based on cloud shape and appearance. The total cumulus cloud cover (for low-altitude clouds, σ_{C_L}) consists of the sum of the covers of forced (σ_{C_F}), active (σ_{C_A}), and passive (σ_{C_P}) cloud covers:

$$\sigma_{C_L} = \sigma_{C_F} + \sigma_{C_A} + \sigma_{C_P} \tag{13.4.1}$$

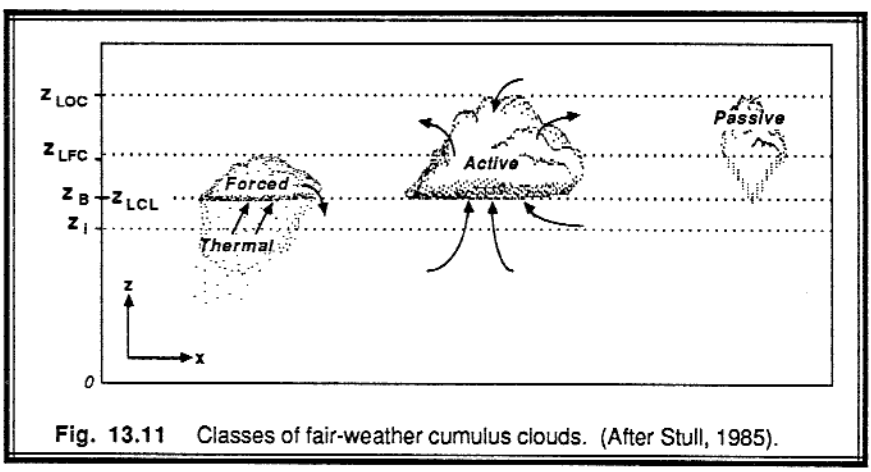

Fig. 13.11 Classes of fair-weather cumulus clouds. (After Stull, 1985).

Forced Clouds. These clouds form in the tops of ML thermals, and exist only while there is continued forcing from the parent thermal. Often, these clouds form in the negatively buoyant portion of the thermal that is overshooting into the capping inversion (entrainment zone). In spite of the latent heat release during condensation, there is insufficient heating for these clouds to become positively buoyant. As a result, the clouds behave as quasi-passive tracers of the top of the thermal. The cloud top never reaches its LFC. Morphologically, these clouds are very shallow and often flat looking, and are usually classified as cumulus humilis.

All of the air rising in the thermal up through the cloud base continues circulating through the cloud and remains within the ML (i.e., there is ***no venting*** of ML air out of the ML). In conditions of light wind shear, air in the cloud diverges from the center toward the lateral edges, where descending return flow into the ML is associated with droplet evaporation. In stronger wind shear, the cloud often appears as a breaking wave, with updrafts on the upshear side, and the return circulation and downdrafts on the downshear side.

Active Clouds. These clouds are also triggered by ML thermals, but at some point a portion of the updraft reaches its LFC and the clouds become positively buoyant. The rising updraft then induces its own pressure perturbations that affect its evolution and draw more air in through its cloud base. The lifetime of this cloud is now controlled by its cloud dynamics and its interaction with the environment. It may persist longer than the ML thermal that first triggered it.

These clouds can ***vent*** ML air out into the FA. Their vertical dimensions are often on the same order, or slightly larger than their horizontal dimensions. Morphologically, they are the cumulus mediocris.

Passive Clouds. When active clouds cease withdrawing air from the ML, we classify them as dynamically passive. The tops of the passive clouds might still be positively buoyant and may even be growing, but they no longer are venting ML air. The bottoms of these clouds are diffuse as the droplets evaporate and mix with the environment. As a result, the original cloud base disappears, leaving the remaining portion of the cloud totally above the ML and EZ where it is not dynamically interactive with the ML.

13.4.2 Feedback from the Clouds to the Mixed Layer

Radiative Feedback. All classes of boundary-layer clouds (σ_{C_L}) shade the surface. Over a land surface this results in negative feedback, because less solar heating of the ground will trigger fewer or weaker thermals and will cause the ML to grow more slowly, resulting in fewer new cumulus clouds being triggered. Thus on days over land where solar heating is the primary driving force for free convection (rather than cold air advection, ground thermal inertia, or forced mechanical convection), fair-weather cumulus clouds will tend to reach an equilibrium cloud cover that is scattered (0.1 to 0.5 coverage) or broken (0.6 to 0.9), but not overcast.

Dynamic Feedback. Active clouds withdraw some of the ML air, causing the ML to grow more slowly or even not grow at all. This negative feedback limits the number of new thermals that can penetrate high enough to trigger new active clouds. The continuity equation (11.2.2b) describes how active clouds can modify ML growth. Given typical values of entrainment velocity, subsidence, cloud base average updraft velocity, and ML growth rate (0.05, -0.01, 1.0, and 0.02 m/s, respectively), (11.2.2b) yields an active cloud cover of 2%. Thus, active clouds rarely cover more than a few percent of the area, even when there are many forced and passive clouds present.

Brümmer and Wendel (1987) observed that these few active clouds have such vigorous vertical motion that their vertical heat and momentum fluxes can be on the order of 100 W/m^2 and 1 N/m^2, respectively. When horizontally averaged over the remainder of the cloud layer, these few clouds were responsible for most of the vertical transport.

Environmental Feedbacks. There are two positive feedbacks that can be easily discussed. Active clouds tend to vent moisture from the ML and deposit it in the FA. Passive clouds tend to evaporate more slowly in a moist FA than in a dry one. Thus, the number of passive and active clouds can increase in the FA with time as new clouds develop, but older passive and active clouds linger because of slower evaporation rates.

Nonprecipitating active clouds also vent some of the cooler ML air (in a potential temperature sense) into the cloud layer. Between clouds, subsidence brings warmer air down to the ML top, where the ML can entrain it. As a result, the ML warms and the FA cools, resulting in a destabilization of the whole ML/FA system and the increase in cloud cover.

13.4.3 Cumulus Onset Time and Cloud Cover

There is a thermal-to-thermal variability in temperature and moisture associated with the variability in land use over which thermals form. Thus, thermals penetrate to a variety of heights, and have a variety of LCLs. The range of penetration heights has already been defined as the entrainment zone. The range of LCLs defines the ***LCL zone*** (Wilde, et al., 1985).

The first cumulus clouds of the day will form when the top of the entrainment zone reaches the bottom of the LCL zone, because at that time some of the thermals are reaching their LCLs. As more of the entrainment zone overlaps and moves above the LCL zone, the cloud cover increases (Fig 13.12). If the entrainment zone were to move completely above the LCL zone, then the sky would be overcast (> 95% cloud cover) because all of the thermals are above their respective LCLs, leaving only the unmixed entrained air as cloud-free breaks in the overcast.

The probability density function (pdf) of finding the top of a thermal at any height within the entrainment zone is well described by a double exponential function, such as is plotted in Fig 13.13. The peak in the function occurs at the mean ML height, z_i, and the width of the function covers the thickness of the entrainment zone. This function indicates

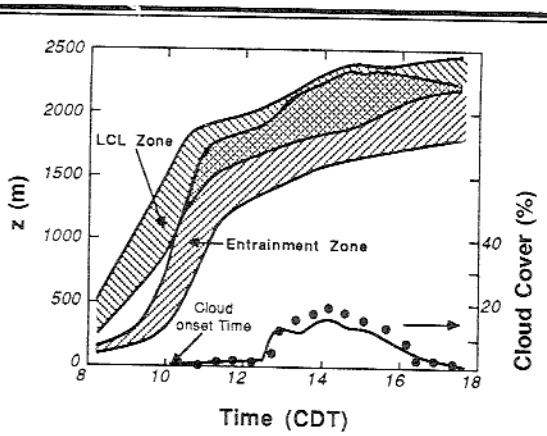

Fig. 13.12 Idealization of the evolution of the entrainment zone and LCL zone, based on BLX83 data. Overlap of these two zones is related to the amount of fair-weather cumulus cloud cover, resulting in a coverage diagnosis sketched at the bottom of the figure. Data points show observed cloud cover for this case. (After Wilde, et al., 1985).

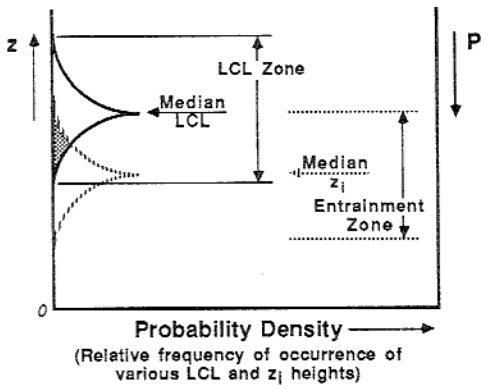

Fig. 13.13 Double exponential shaped probability distribution functions for both the LCL zone and the entrainment zone. Forced-cloud cover is related to the convolution between both distributions. (After Wilde, et al., 1985).

that the tops of thermals are more likely to be found near z_i, and less likely further away. A similar double exponential pdf describes the distribution of LCLs.

By integrating over both pdfs for the entrainment zone and the LCL zone, we can determine the cloud cover of forced clouds from the total probability of finding thermals above their LCLs (Wilde, et al., 1985):

$$\sigma_{C_F} = \int_{z_i = 0}^{\infty} \text{pdf}(z_i) \int_{z_{LCL} = 0}^{z_i} \text{pdf}(z_{LCL})\ dz_{LCL}\ dz_i \qquad (13.3.3)$$

To forecast coverage of active and passive clouds, one must develop prognostic equations such as those by Rogers, et al. (1985a).

13.4.4 Cloud Size Distribution

Lopez (1977) demonstrated that many cloud attributes, such as diameter and depth, are distributed lognormally. Examples of observed cloud size distributions are shown in Fig 13.14, along with the best fit lognormal curve (Stull, 1984). We see that the diameters and depths of most clouds cluster together, but there is a small percentage of clouds that are much larger.

The expression for a lognormal distribution is given by:

$$\text{pdf}(X) = \frac{1}{(2\pi)^{1/2}\ X\ S_X} \exp\left[-0.5 \left(\frac{\ln(X/L_X)}{S_X} \right)^2 \right] \qquad (13.4.4)$$

where L_X and S_X are the location and shape parameters, and X represents diameter or depth. Integrating (13.3.4) over all X yields 1.0, which means that 100% of the clouds present are explained.

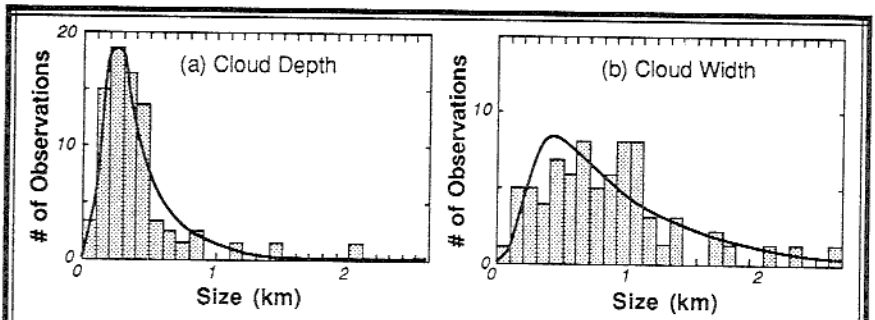

Fig. 13.14 Histograms of (a) cloud depth, and (b) cloud width, as measured from an airborne forward-looking automatic camera system. A total of 78 fair-weather cumulus were observed during this one BLX83 case. The smooth curve is a maximum-likelihood best fit of a lognormal distribution function to the data. (After Stull, 1984).

13.4.5 Profiles of Mean Variables and Fluxes

Examples of soundings in a variety of cloudy boundary layers over oceans and continents for different thermodynamic variables are shown in Figs 13.15 to 13.17. Bougeault (1982) produced idealized profiles of liquid water potential temperature and total water mixing ratio (Fig 13.15) using data from the Puerto Rico, Voves, and GATE field experiments. The Puerto Rican data was obtained over the western tropical Atlantic (Pennell and LeMone, 1974), where there was a strong capping ***trade-wind inversion*** at 1.5 km, strong (15 m/s) BL winds, and vigorous turbulence generation (primarily by shear in the lower third of the BL). The suppressed cumulus clouds in this region are called ***trade-wind cumuli***.

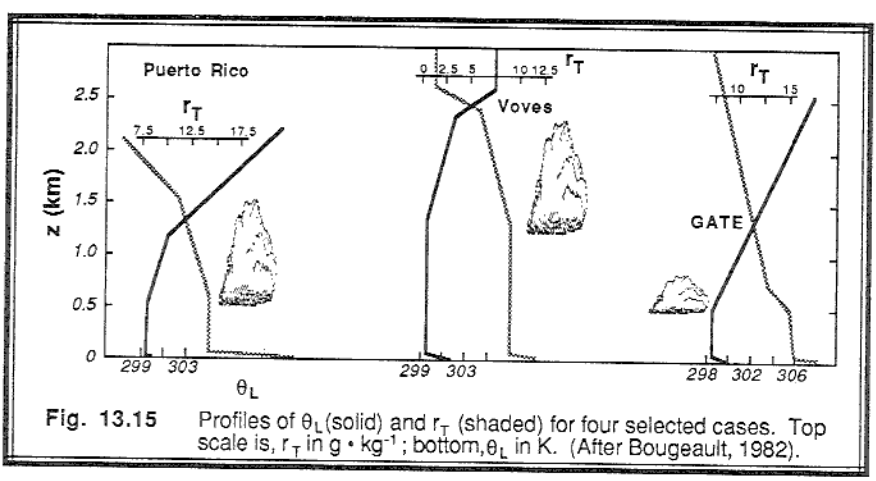

Fig. 13.15 Profiles of θ_L (solid) and r_T (shaded) for four selected cases. Top scale is, r_T in g • kg^{-1}; bottom, θ_L in K. (After Bougeault, 1982).

The GATE data was obtained over the eastern tropical Atlantic (Nicholls and LeMone, 1980), where light winds (3 to 5 m/s) and cooler sea surface temperatures resulted in weaker mixing of the BL. The trade-wind inversion was at lower altitudes in the GATE area (e.g., at about 750 m), and longwave radiative cooling of the BL approximately balanced convective heating. Both the Puerto Rican and GATE data exhibited mesoscale variability in cloudiness, and both had suppressed, nonprecipitating cumulus clouds. The Voves data was taken over central France during the summer, where stronger convection and weaker environmental stability resulted in a deeper boundary layer with taller cumulus clouds.

Betts and Albrecht (1987) show a selected set of soundings from over the equatorial Pacific Ocean obtained during the 1979 FGGE experiment (Fig 13.16). This diagram represents an average of 84 individual soundings, where only those soundings having active clouds capped by an inversion below 60 kPa (600 mb) are included. The vertical line rising from the θ_e curve represents the adiabatic rise of a parcel starting from 98 kPa (980 mb), and indicates positive buoyancy (where it is warmer than the θ_{es} curve) between about 95 and 85 kPa (950 and 850 mb). The capping inversion is enhanced by subsidence, but is also modified by radiative cooling.

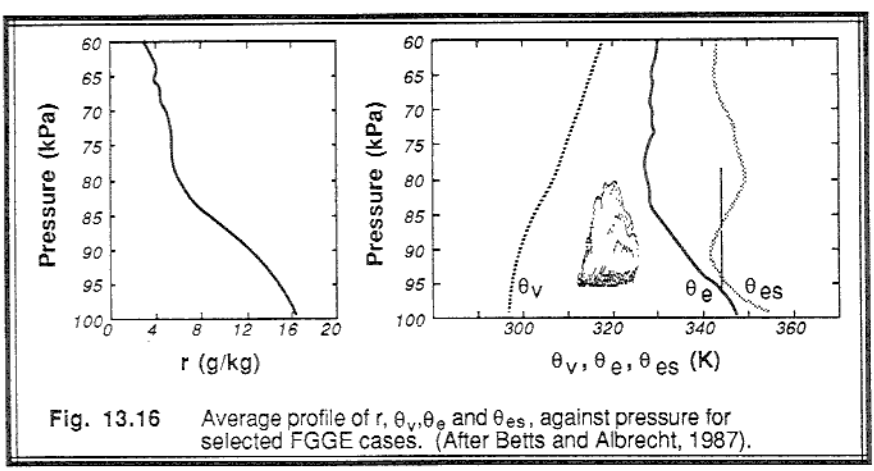

Fig. 13.16 Average profile of r, θ_v,θ_e and θ_{es}, against pressure for selected FGGE cases. (After Betts and Albrecht, 1987).

Finally, Raymond and Blyth (1986) show potential temperature, equivalent potential temperature, and parcel buoyancy ($g \cdot \Delta\theta_v/\theta_v$) for nonprecipitating towering cumulus clouds observed over the Magdalena Mountains of New Mexico (Fig 13.17). Weak cold frontal passage earlier in the day reduced the instability of the lower atmosphere, preventing thunderstorm development.

Examples of fluxes and variances averaged horizontally are shown in Fig 13.18, based on the analysis of Nicholls, et al. (1982). We find significantly large variances, particularly of temperature, within the cloud layer. Nicholls and LeMone (1980) found that clouds affect the distribution of heat and moisture within the subcloud layer, but had

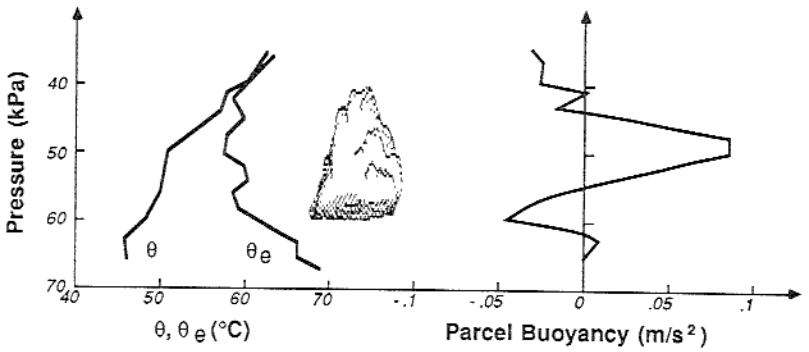

Fig. 13.17 Soundings for towering cumuli on 29 July 1980 over New Mexico. (After Raymond and Blyth, 1986).

little effect on the buoyancy profile. The greatest coupling between the cloud and subcloud layers was via large wavelengths rather than small. Soong and Ogura (1980) determined that cumulus clouds tend to respond rapidly to changes in large-scale forcings, and can be assumed to be in a state of quasi-equilibrium.

Betts (1973) suggests that vertical fluxes associated with cumulus convection can be parameterized using the concept of a ***convective mass flux***, ω^*, where $\omega^* = \sigma_{C_A} \cdot w_{up}$, and where w_{up} is the average vertical velocity through the cloud bases of all active clouds. The fluxes of any conserved variable, ξ, can be written as:

$$\overline{w'\xi'} = \frac{\omega^* (\xi_{up} - \bar{\xi})}{1 - \sigma_{C_A}} \qquad (13.4.5a)$$

$$\overline{w'\xi'} = \omega^* (\xi_{up} - \xi_{down}) \qquad (13.4.5b)$$

where subscripts up and down represent the updraft and downdraft portions of the cloud circulation, and the overbar represents a horizontal average over both cloud and environmental air. Penc and Albrecht (1987) find that this convective mass flux approach also works fairly well for stratocumulus clouds, where they estimate $\omega^* = 0.1$ m/s near the base of the cloud, decreasing slightly with height for the cases they examined.

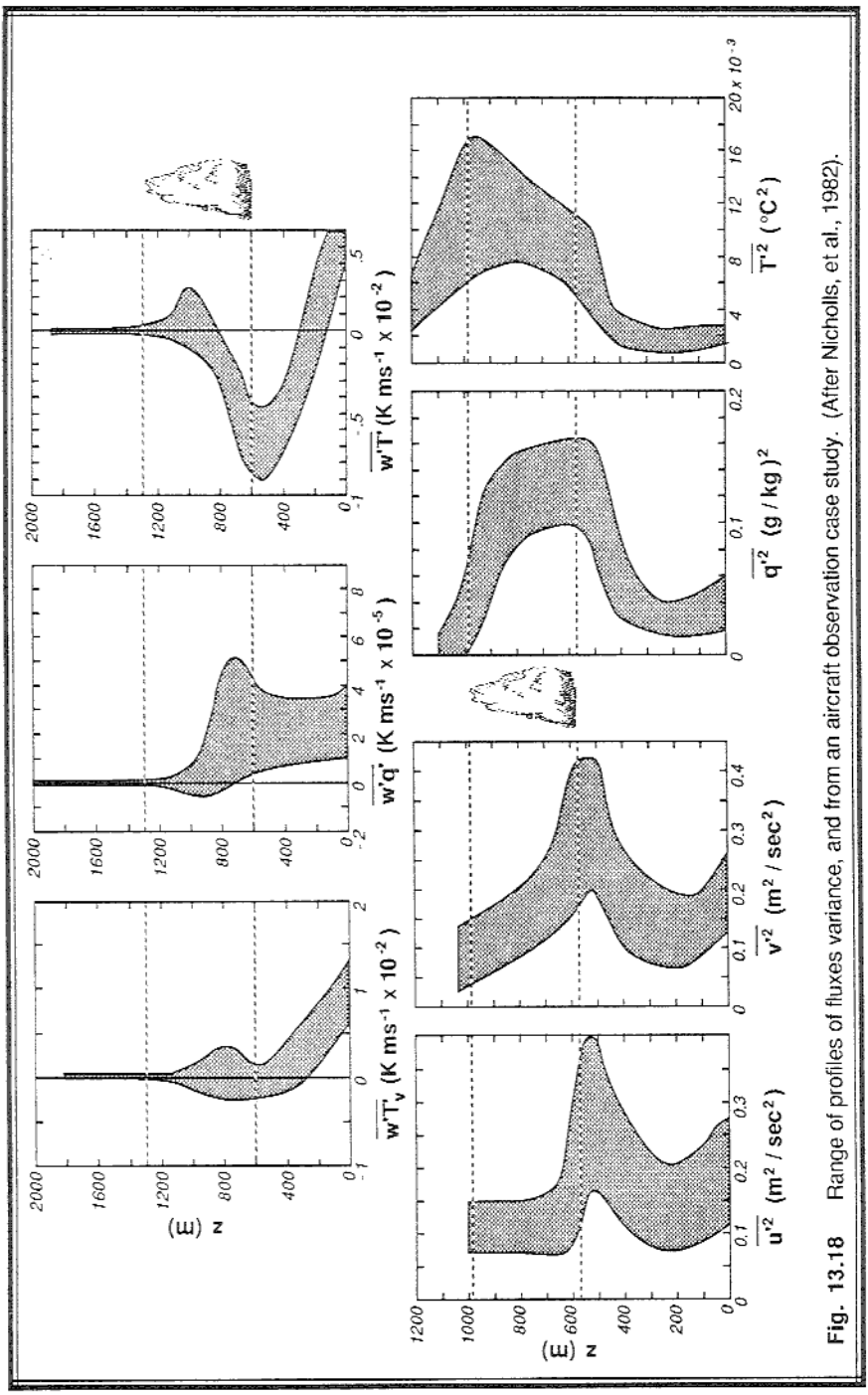

Fig. 13.18 Range of profiles of fluxes variance, and from an aircraft observation case study. (After Nicholls, et al., 1982).

13.5 Stratocumulus

13.5.1 Vertical Profiles of Mean Variables and Fluxes

Fig 13.19 shows an idealized composite of vertical profiles of mean variables through a stratocumulus topped mixed layer, in which the cloud and subcloud layers are fully turbulently coupled (Turton and Nicholls, 1987; Rogers and Telford, 1986; Albrecht, et al., 1985; Roach, et al., 1982; Caughey, et al., 1982; Slingo, et al., 1982; Brost, et al., 1982a; and Stage and Businger, 1981a).

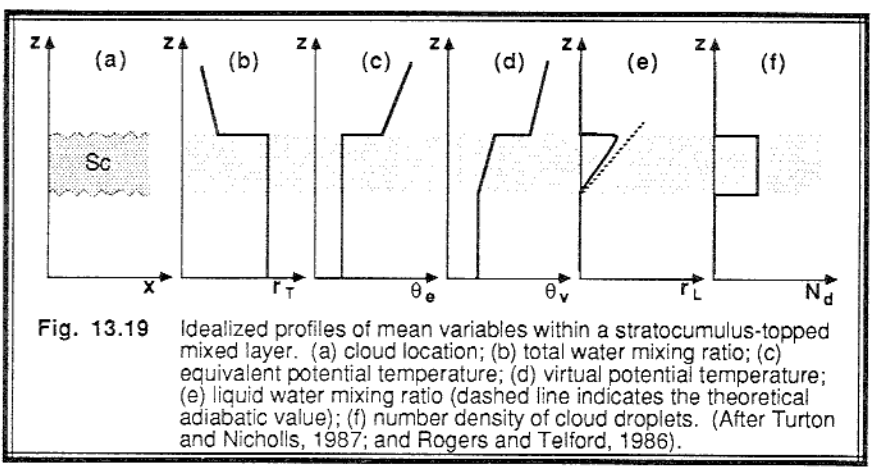

Fig. 13.19 Idealized profiles of mean variables within a stratocumulus-topped mixed layer. (a) cloud location; (b) total water mixing ratio; (c) equivalent potential temperature; (d) virtual potential temperature; (e) liquid water mixing ratio (dashed line indicates the theoretical adiabatic value); (f) number density of cloud droplets. (After Turton and Nicholls, 1987; and Rogers and Telford, 1986).

The equivalent potential temperature and total water mixing ratio are constant with height, supporting the view that the stratocumulus clouds are imbedded within, and are an integral part of, the ML. The virtual potential temperature follows the moist adiabat within the cloud layer, and the liquid water content increases almost linearly with height above cloud base as would be expected if there were no precipitation. Variations in liquid water content (or mixing ratio) are expected due to entrainment of drier air from above. The top of the cloud often has significantly less liquid water than expected, for the same reason. The number density of drops is roughly constant, however, suggesting that the droplets are larger near the top of the cloud.

Turbulent flux responses to various imposed forcings are shown in Fig 13.20 (a-e), where the solid lines indicate the response for a fully coupled cloud and subcloud BL, and the dashed lines show the response for a cloud layer just recently decoupled from the subcloud layer at cloud base. Figs 13.20 a & b show the individual effects of surface heating and entrainment, while Figs 13.20 c-e show individual responses to both IR and solar radiation. These individual curves are analogous to the process-partitioning results for TKE production and consumption. For the entrainment curve, it is assumed for the decoupled case that the cloud and subcloud layers are independently turbulent, with entrainment in both directions across the interface at cloud base.

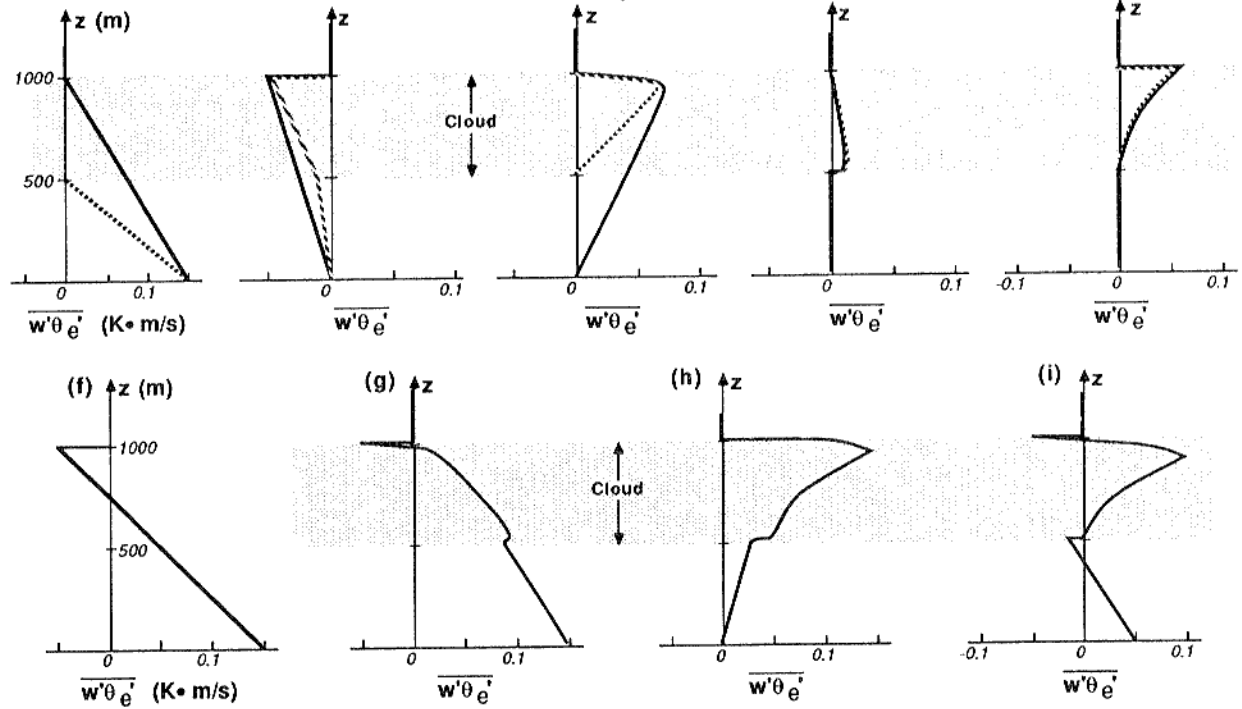

Fig. 13.20 Idealized cloud-process components are sketched in (a) through (e) for coupled (solid) and uncoupled (dashed) cloud and subcloud layers. These can be combined to make profiles for more realistic scenarios: (f) cloud-free ML; (g) entraining nocturnal BL over a warm surface; (h) daytime BL, no entrainment, no surface heating; and (i) decoupled daytime BL.

These five figures can be used as building blocks to construct the turbulence response for more complex cases. For example, adding (a) and (b) yields the usual linear ML heat flux profile (Fig 13.20f). Adding (a) thru (d) gives a profile for an entraining nocturnal stratocumulus-topped BL over a warm surface (Fig 13.20g) that looks similar to the data from Stage and Businger (1981). Adding only the radiative contributions yields the response shown in Fig 13.20h, which is similar to the transilient simulations of Stull and Driedonks (1987). Finally, the sum of all components (a-e) for the decoupled case yields a curve (Fig 13.20i) resembling the data of Turton and Nicholls (1987). Similar constructions can be made to simulate the data of Nicholls and Leighton (1986), Albrecht, et al. (1985), Brost, et al. (1982b), and Deardorff (1980). For all of these cases there are noticable changes in many of the turbulent fluxes near cloud top and cloud base, corresponding to changes in the radiative forcing.

13.5.2 Mixing Processes

There are seven processes that can generate the mixing required to maintain stratocumulus clouds: surface-based (free) convection, differential cold-air advection, surface-layer shear (forced convection), cloud-top radiative cooling, cloud-base radiative heating, cloud-layer shear, and cloud-top entrainment instability. All of these are processes that can be maintained in the absence of strong solar heating of the ground, because we are assuming a broken to overcast stratocumulus deck that shades the ground and attenuates the incoming solar radiation. Also, many of the processes can operate simultaneously.

Surface-based free convection occurs when cold air is advecting over a warmer surface, such as immediately following a cold front passage over land, or cold air masses moving over warmer lakes or ocean currents. The first situation is usually temporary, and disappears as either drier air advects in, or as the heat stored in the ground is lost. The second situation is sometimes seasonal, and is associated with semi-stationary fog and stratocumulus features such as the stratocumulus clouds off of southern California, or the snow squalls downwind of the Great Lakes.

Differential cold-air advection. Sometimes after a cold frontal passage, colder air is advected into an area aloft than is advected in at lower levels. The result is a static destabilization of the layer of air, causing convection and cloud formation. Such destabilization can occur even when the surface is colder than the overlying air.

Shear-generated mechanical turbulence associated with strong BL winds can also cause sufficient mixing (forced convection) to maintain the stratocumulus topped ML. Strong winds and the associated surface-layer shear are also found near fronts and low pressure centers.

Cloud-top radiative cooling creates upside-down "thermals" of cold air that sink from cloud top. This is another form of free convection, and can be important when there are not other higher cloud decks to reduce the infrared cooling from the lowest deck. This process can operate both day and night.

Cloud-base radiative heating is usually much weaker than cloud top cooling, because of the small absolute temperature difference between the cloud-base and the surface. This process differs from the preceeding ones because it destabilizes the cloud layer, but stabilizes the subcloud layer. If conditions are right, cloud-base heating can contribute to the decoupling of the cloud and subcloud layers.

Cloud-layer shear generates mechanical turbulence and mixing. Usually, the shear is found near cloud top, although it is less frequently found near cloud base. The turbulence generated by cloud-top shear generates very localized mixing and entrainment, and can also contribute to decoupling of the cloud layer from the subcloud layer unless there are other turbulent processes that can mix the excess TKE throughout the whole ML.

Cloud-top entrainment instability was descibed earlier, and is associated with entrainment that leads to free convection of cold descending air parcels. Given the proper ambient conditions at cloud top and the appropriate trigger, this process usually dries and warms the ML, causing the cloud-base height to rise and the cloud deck to break up.

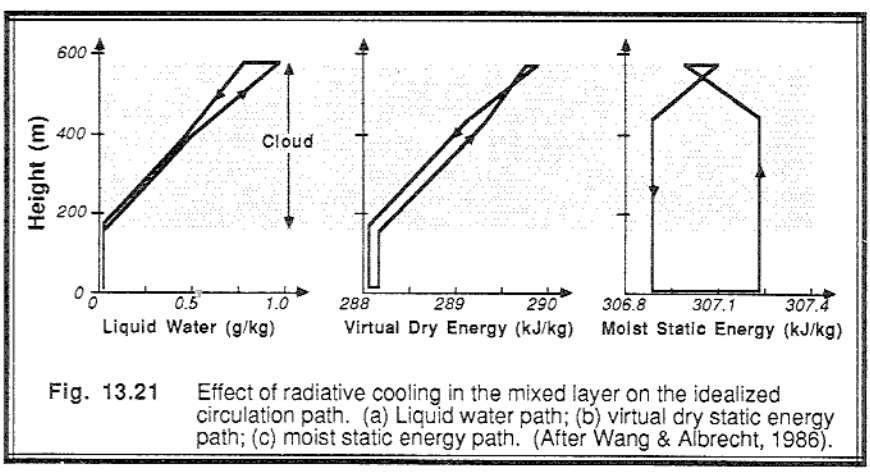

Fig. 13.21 Effect of radiative cooling in the mixed layer on the idealized circulation path. (a) Liquid water path; (b) virtual dry static energy path; (c) moist static energy path. (After Wang & Albrecht, 1986).

Both the Eulerian and process partitioning of the TKE budget have been used to study mixing in stratocumulus clouds. Some of the Eulerian methods are discussed in the next subsection. Wang and Albrecht (1986) used a process approach to model the updraft and downdraft portions of the mixing circulations directly. A sample of their modeled updraft and downdraft paths is shown in Fig 13.21, where they found that the thermodynamic differences between the two paths is much less than the differences between the cloud and its environment.

Moeng (1987) analyzed her large-eddy simulation model by grouping the warm rising and cold sinking air parcels into a process-production component of TKE, and the warm sinking and cold rising parcels into the process-consumption component. She found that consumption is a larger fraction (0.22) of the total production (buoyant and shear) of TKE for cloud-topped MLs than for cloud-free MLs, where the fraction was only 0.15 (see Fig 13.22). Moeng also confirmed that most (85%) of the longwave radiative cooling occurs near the top edge of the cloud, in the entrainment zone portion of the BL.

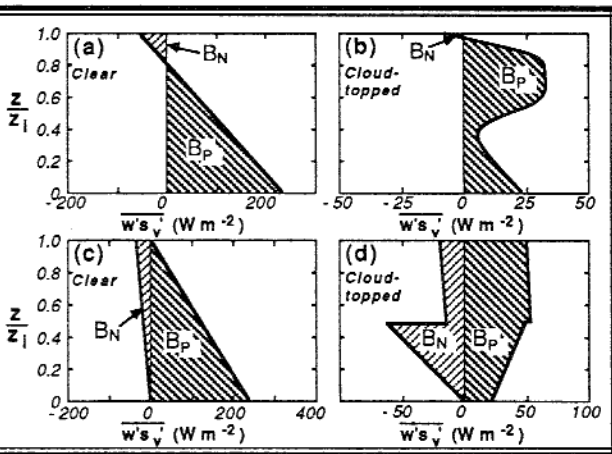

Fig. 13.22 Simulation of production (B_P) and consumption (B_N) for: (a & b) Eulerian partioning, and (c & d) process partioning. (After Moeng, 1987).

13.5.3 Processes for Decoupling

During the day when solar heating of the cloud is significant, if the surface heat flux is small, then it is possible for turbulence in the cloud layer to become decoupled from turbulence in the bottom of the subcloud layer, with a stable transition layer in between (Turton and Nicholls, 1987; Nicholls and Leighton, 1986). For this situation, TKE production is too weak to support the large TKE consumption associated with downward mixing of heated cloud-layer air into the subcloud layer.

Using the Eulerian definition for production and consumption, Turton and Nicholls require that the net consumption below cloud base be less than a fraction of the net production above cloud top, where z_L is the height of the bottom of the cloudy ML:

$$\int_{z_L}^{z_B} \overline{w'\theta_v'}\, dz \;<\; -0.4 \int_{z_B}^{z_T} \overline{w'\theta_v'}\, dz \qquad (13.5.3a)$$

It this condition is satisfied for $z_L = 0$, then the cloud and subcloud layers are fully coupled. Otherwise, decoupling is suggested with $z_L > 0$ in order to satisfy (13.5.3a).

Fig 13.23 shows examples of fully coupled and uncoupled layers. A fully coupled mixed layer can become decoupled after sunrise when there is sufficient heating within the cloud layer. The two layers can stay decoupled if there is sufficient cloud heating, or can become recoupled near sunset when the cloud heating is removed (see Fig 13.24).

Other mechanisms can also cause decoupling. If cloud-top entrainment instability entrains sufficient warm air into the top of the cloud layer, then decoupling can occur (Rogers, et al., 1985a). Decoupling is also possible when shear generation of turbulence at the top of the cloud layer is large enough (Wai, 1987).

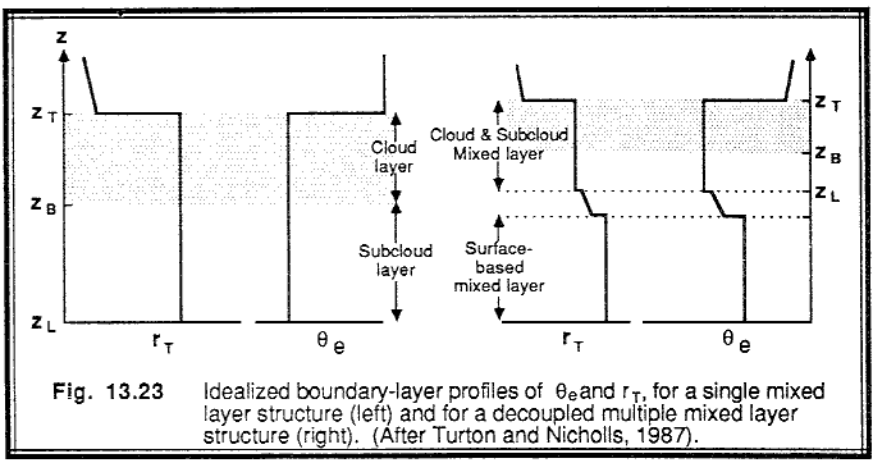

Fig. 13.23 Idealized boundary-layer profiles of θ_e and r_T, for a single mixed layer structure (left) and for a decoupled multiple mixed layer structure (right). (After Turton and Nicholls, 1987).

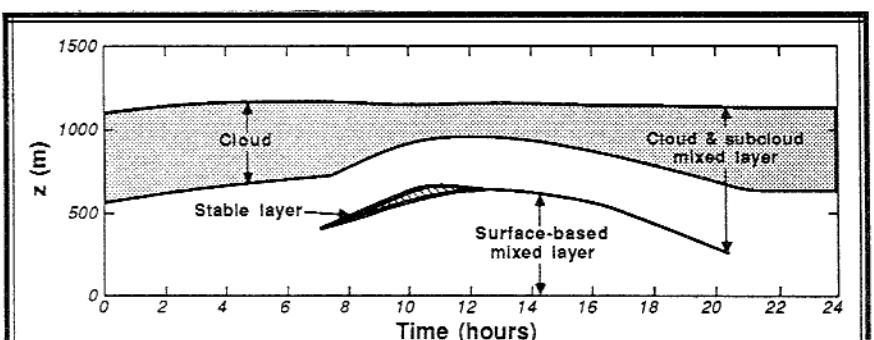

Fig. 13.24 Simulated diurnal evolution of the cloud layer for mid-latitude stratocumulus in summer, showing a decoupling into two separate mixed layers in late morning and afternoon. (After Turton and Nicholls, 1987).

13.5.4 Entrainment

Most of the cloud-top entrainment relationships are written as a balance between the production, dissipation, and consumption of TKE (Stage and Businger, 1981). The production mechanisms include surface heating, cloud-top cooling, cloud-top entrainment instability, and wind shear. Consumption is associated with warm entrained air moving down and cold air moving up. The basic premise, as discussed in Section 11.4.3, is that the portion of produced TKE which is not dissipated or transported away can be expended by consumption during the entrainment process.

Randall (1984) recognized that entrainment and parcel motion is a very nonlocal process that is best described by Lagrangian or nonlocal turbulence closure approaches. Parameterizations of the Lagrangian concept lead to the Eulerian and process partitioning

approximations described earlier, but variations in the particular choice of parameterization can lead to estimates of entrainment differing by over a factor of two. It is clear that more work needs to be done to clarify the cloud-top entrainment process in stratocumulus (Hanson, 1984).

Some specialized entrainment models have also been proposed based on a limited set of production mechanisms. For example, Rogers, et al. (1985a) suggested the following entrainment velocity for cloud-top entrainment instability :

$$w_e \cong \left[\frac{g}{\theta} \left| \Delta_{EZ} \theta_e \right| l_c \right]^{1/2} \tag{13.5.4a}$$

where l_c is the distance traveled by negatively buoyant entrained elements. When cloud-top radiative cooling dominates:

$$w_e \cong \frac{\Delta I^*}{\Delta_{EZ} \theta_v} \tag{13.5.4b}$$

where ΔI^* is the net longwave radiative flux divergence near cloud top, expressed in kinematic units (K m/s). Other buoyancy flux production factors have been used in the numerator of the above equation for processes other than radiation.

Finally, many entrainment relationships have been proposed relating a dimensionless entrainment velocity to an inverse Richardson number (Nicholls and Turton, 1986):

$$\frac{w_e}{w_* \text{ or } u_*} \propto Ri^{*-1} \tag{13.5.4c}$$

where the convective Richardson number, Ri^*, can be defined in terms of w_*, u_*, or other turbulence production scales. Deardorff (1980; and Albrecht, et al., 1985) suggest that critical values of the entrainment velocity can be related to stratocumulus breakup and dissipation. Tag and Payne (1987) note that stratocumulus decks can break up slower in stronger wind shears at cloud top, given that the cloud-top entrainment instability criterion is satisfied.

13.6 Fog

The following fog types can form in the boundary layer: radiation, advection, precipitation (frontal), steam, and upslope. Only the first two will be discussed in more detail here.

13.6.1 Radiation Fog

Two types of radiation fog have been observed: (1) a mist that is most dense near the ground but becomes diffuse with height; and (2) a well-mixed fog layer with a sharp top

that is similar to a stratocumulus cloud (Welch and Wielicki, 1986; and Gerber, 1981). The following scenario shows how these fogs develop, and how the mist can become a well-mixed fog (Wessels, personal communication).

As the air close to the ground cools further below the dew point temperature than air higher in the SBL, a mist can form that sometimes has greater liquid water content at the bottom than the top (Gerber, 1981). This fog has a diffuse top and is often very shallow, with depths from 1 m to about 5 m (Fig 13.25a). If the sun rises before this fog develops further, then short-wave radiation can penetrate the fog, heat the surface, and evaporate the fog. SBL scaling and dynamics can be used to describe this fog.

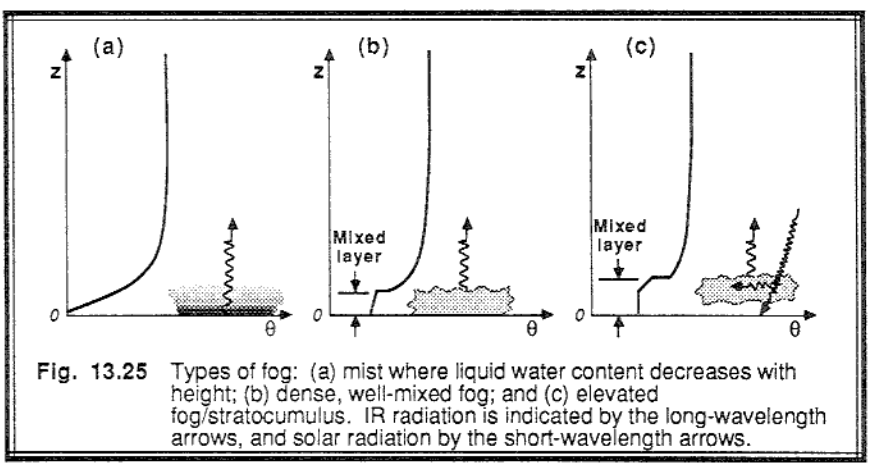

Fig. 13.25 Types of fog: (a) mist where liquid water content decreases with height; (b) dense, well-mixed fog; and (c) elevated fog/stratocumulus. IR radiation is indicated by the long-wavelength arrows, and solar radiation by the short-wavelength arrows.

Instead, if the mist thickens and liquid water content increases during the night as radiative cooling continues, then there is less net radiative heat loss from the ground and more from the dense parts of the fog. Eventually, the fog becomes optically thick enough that there is greater radiative flux divergence near the top of the fog than the bottom. At this point, cooling at fog top generates cold thermals that sink and begin to convectively mix the fog layer. Very quickly, the fog becomes more uniform in the vertical, with a well-defined top edge (Fig 13.25b). This sharp top also concentrates the radiative divergence closer to that region, which reinforces convective mixing in the fog layer.

The well-mixed fog behaves like a stratocumulus cloud, and can consists of cellular circulation patterns or patches with a horizontal scale on the order of 2 to 3 times the fog depth (Welch and Ravichandran, 1985; and Welch and Wielicki, 1986). Both the well-mixed fog and the stratocumulus cloud appear to follow convective ML scaling (using turbulent fluxes at the top of the ML where appropriate) rather than SBL scaling. Many of the parameterizations described earlier in this chapter for stratocumulus clouds can be applied to the well-mixed fog.

Well-mixed fog can persist well into the morning, because much of the solar radiation is reflected from the top, and radiative cooling of the top continues during the day. The combined effects of absorption of a little solar radiation in the interior of the fog and

longwave cooling at cloud top can cause the boundary layer to warm and the fog base to *lift* from the ground. This fog is then reclassified as a stratocumulus cloud (Fig 13.25c). Sometimes the patchiness of the fog is enhanced by solar heating of the ground between patches, causing the fog to break up into cumulus clouds. A wind-speed increase can also enhance mixing of the fog with drier, warmer air aloft to trigger fog lifting or break-up.

The onset time of fog, and the transition from a mist to a well-mixed fog, are sensitive to the balance between all processes (Turton and Brown, 1987). Small errors in any one of the processes can lead to large errors in fog forecasts and models. As a result, precise onset and dissipation times for fog are often difficult to forecast.

13.6.2 Advection Fog

Advection of warm humid air over a cooler surface can result in advection fog. Such fogs are frequently found off the west coast of California, and the west coasts of South America. With persistent wind fields and sea surface temperature, it is relatively easy to forecast the onset location and mean properties of this fog. Advection fogs are also found during spring when warm, moist air advects over snow and cold lake surfaces. Forecast methods utilize SBL and TIBL evolution physics.

Once formed, radiative cooling of the fog top can enhance the mixing, creating the stratocumulus-like advection fog with a sharp top. Light winds can also induce sufficient mixing to create a cool ML filled with advection fog.

13.7 References

Albrecht, B.A., R.S. Penc and W.H. Schubert, 1985: An observational study of cloud-topped mixed layers. *J. Atmos. Sci.*, **42**, 800-822.

Anderson, D.L.T., 1976: The low-level jet as a western boundary current. *Mon. Wea. Rev.*, **104**, 907-921.

Betts, A.K., 1973: Non-precipitating cumulus convection and its parameterization. *Quart. J. Roy. Meteor. Soc.*, **99**, 178-196.

Betts, A.K., 1982a: Saturation point analysis of moist convective overturning. *J. Atmos. Sci.*, **39**, 1484-1505.

Betts, A.K., 1982b: Cloud thermodynamic models in saturation point coordinates. *J. Atmos. Sci.*, **39**, 2182-2191.

Betts, A.K., 1983: Thermodynamics of mixed stratocumulus layers: saturation point budgets. *J. Atmos. Sci.*, **40**, 2655-2670.

Betts, A.K., 1985: Mixing line analysis of clouds and cloudy boundary layers. *J. Atmos. Sci.*, **42**, 2751-2763.

Betts, A.K., 1986: A new convective adjustment scheme. I: observations and theoretical basis. *Quart. J. Roy. Meteor. Soc.*, **112**, 677-692.

Betts, A.K. and B.A. Albrecht, 1987: Conserved variable analysis of the convective boundary layer thermodynamic structure over tropical oceans. *J. Atmos. Sci.*, **44**, 83-99.

Betts, A.K. and M.J. Miller, 1986: A new convective adjustment scheme. II: single column test using GATE wave, BOMEX, and arctic air-mass data sets. *Quart. J. Roy. Meteor. Soc.*, **112**, 693-710.

Blyth, A.M. and J. Latham, 1985: An airborne study of vertical structure and microphysical variability within small cumulus. *Quart. J. Roy. Meteor. Soc.*, **111**, 773-792.

Boatman, J.F. and A.H. Auer, Jr., 1983: The role of cloud-top entrainment in cumulus clouds. *J. Atmos. Sci.*, **40**, 1517-1534.

Bolton, D., 1980: The computation of equivalent potential temperature. *Mon. Wea. Rev.*, **108**, 1046-1053.

Bougeault, P., 1982: Cloud-ensemble relations based on the gamma probability distribution for the higher-order models of the planetary boundary layer. *J. Atmos. Sci.*, **39**, 2691-2700.

Bougeault, P., 1985: The diurnal cycle of the marine stratocumulus layer: a higher-order model study. *J. Atmos. Sci.*, **42**, 2826-2843.

Brümmer, B. and M. Wendel, 1987: Observations of intermittent cumulus convection in the boundary layer. *Quart. J. Roy. Meteor. Soc.*, **113**, 19-36.

Buck, A.L., 1981: New equations for computing vapor pressure and enhancement factor. *J. Appl. Meteor.*, **20**, 1527-1532.

Caughey, S.J., B.A. Crease, and W.T. Roach, 1982: A field study of nocturnal stratocumulus: II. turbulence structure and entrainment. *Quart. J. Roy. Meteor. Soc.*, **108**, 125-144.

Curry, J.A., 1986: Interactions among turbulence, radiation and microphysics in arctic stratus clouds. *J. Atmos. Sci.*, **43**, 90-106.

Deardorff, J.W., 1976: On the entrainment rate of a stratocumulus-topped mixed layer. *Quart. J. Roy. Meteor. Soc.*, **102**, 563-582.

Deardorff, J.W., 1980: Cloud-top entrainment instability. *J. Atmos. Sci.*, **37**, 131-147.

Eymard, L., 1984: Radar analysis of a tropical convective boundary layer with shallow cumulus clouds. *J. Atmos. Sci.*, **41**, 1380-1393.

Fravalo, C., Y. Fouquart and R. Rosset, 1981: The sensitivity of a model of low stratiform clouds to radiation. *J. Atmos. Sci.*, **38**, 1049-1062.

Gerber, H.E., 1981: Microstructure of a radiation fog. *J. Atmos. Sci.*, **38**, 454-458.

Hignett, P., 1987: A study of the short-wave radiative properties of marine stratus: aircraft measurements and model comparisons. *Quart. J. Roy. Meteor. Soc.*, **113**, 1011-1024.

Hanson, H.P., 1984: On mixed layer modeling of the stratocumulus-topped marine boundary layer. *J. Atmos. Sci.*, **41**, 1226-1234.

Hanson, H.P., 1987: Radiative/turbulent transfer interactions in layer clouds. *J. Atmos. Sci.*, **44**, 1287-1295.

Hanson, H.P. and V.E. Derr, 1987: Parameterization of radiative flux profiles within layer clouds. *J. Clim. Appl. Meteor.*, **26**, 1511-1521.

Jensen, J.B., P.H. Austin, M.B. Baker and A.M. Blyth, 1985: Turbulent mixing, spectral evolution and dynamics in a warm cumulus cloud. *J. Atmos. Sci.*, **42**, 173-192.

Kitchen, M. and S.J. Caughey, 1981: Tethered balloon observations of the structure of small cumulus clouds. *Quart. J. Roy. Meteor. Soc.*, **107**, 853-874.

Lilly, D.K., 1968: Models of cloud-topped mixed layers under a strong inversion. *Quart. J. Roy. Meteor. Soc.*, **94**, 292-309.

Lopez, R.E., 1976: The lognormal distributions and cumulus cloud population. *Mon. Wea. Rev.*, **105**, 1865-1872.

Lowe, P.R., 1977: An approximating polynomial for the computation of saturation vapor pressure. *J. Appl. Meteor.*, **16**, 100-103.

Moeng, C.-H., 1987: Large-eddy simulation of a stratus-topped boundary layer. Part II. Implications for mixed-layer modeling. *J. Atmos. Sci.*, **44**, 1605-1614.

Moeng, C.-H. and D.A. Randall, 1984: Problems in simulating the stratocumulus-topped boundary layer with a third-order closure model. *J. Atmos. Sci.*, **41**, 1588-1600.

Nicholls, S., 1984: The dyamics of stratocumulus: aircraft observations and comparisons with a mixed layer model. *Quart. J. Roy. Meteor. Soc.*, **110**, 783-820.

Nicholls, S. and J. Leighton, 1986: An observational study of the structure of stratiform cloud sheets. Part I. Structure. *Quart. J. Roy. Meteor. Soc.*, **112**, 431-460.

Nicholls, S. and M.A. LeMone, 1980: The fair-weather boundary layer in GATE: The relationship of subcloud fluxes and structure to the distribution and enhancement of cumulus clouds. *J. Atmos. Sci.*, **37**, 2051-2067.

Nicholls, S., M.A. LeMone and G. Sommeria, 1982: The simulation of a fair-weather marine boundary layer in GATE using a three-dimensional model. *Quart. J. Roy. Meteor. Soc.*, **108**, 167-190.

Nicholls, S. and J.D. Turton, 1986: An observational study of the structure of stratiform cloud sheets. Part II. Entrainment. *Quart. J. Roy. Meteor. Soc.*, **112**, 461-480.

Paluch, I.R., 1979: The entrainment mechanism in Colorado cumuli. *J. Atmos. Sci.*, **36**, 2467-2478.

Penc, R.S. and B.A. Albrecht, 1987: Parameteric representation of heat and moisture fluxes in cloud-topped mixed layers. *Bound.-Layer Meteor.*, **38**, 225-248.

Pennell, W.T. and M.A. LeMone, 1974: An experimental study of turbulence structure in the fair-weather trade wind boundary layer. *J. Atmos. Sci.*, **31**, 1308-1323.

Pontikis, C., A. Rigaud and E. Hicks, 1987: Entrainment and mixing as related to the microphsical properties of shallow warm cumulus clouds. *J. Atmos. Sci.*, **44**, 2150-2165.

Randall, D.A., 1980: Conditional instability of the first kind upside down. *J. Atmos. Sci.*, **37**, 125-130.

Randall, D.A., 1984: Buoyant production and consumption of turbulence kinetic energy in cloud-topped mixed layers. *J. Atmos. Sci.*, **41**, 402-413.

Randall, D.A., J.A. Coakley, Jr., C.W. Fairall, R.A. Kropfli, and D.H. Lenschow, 1984: Outlook for research on subtropical marine stratiform clouds. *Bull. Amer. Meteor. Soc.*, **65**, 1290-1301.

Randall, D.A. and G.J. Huffman, 1982: Entrainment and detrainment in a simple cumulus cloud model. *J. Atmos. Sci.*, **39**, 2793-2806.

Raymond, D.J. and A.M. Blyth, 1986: A stochastic mixing model for nonprecipitating cumulus clouds. *J. Atmos. Sci.*, **43**, 2708-2718.

Raymond, D.J. and M.H. Wilkening, 1982: Flow and mixing in New Mexico mountain cumuli. *J. Atmos. Sci.*, **39**, 2211-2228.

Roach, W.T., R. Brown, S.J. Caughey, B.A. Crease and A. Slingo, 1982: A field study of nocturnal stratocumulus. I. Mean structure and budgets. *Quart. J. Roy. Meteor. Soc.*, **108**, 103-124.

Rogers, D.P., J.A. Businger, and H. Charnock, 1985a: A numerical investigation of the JASIN atmospheric boundary layer. *Bound.-Layer Meteor.*, **32**, 373-399.

Rogers, D.P. and J.W. Telford, 1986: Metastable stratus tops. *Quart. J. Roy. Meteor. Soc.*, **112**, 481-500.

Rogers, D.P., J.W. Telford and S.K. Chai, 1985b: Entrainment and the temporal development of the microphysics of convective clouds. *J. Atmos. Sci.*, **42**, 1846-1858.

Schmetz, J. and M. Beniston, 1986: Relative effects of solar and infrared radiation forcing in a mesoscale model. *Bound.-Layer Meteor.*, **34**, 137-155.

Slingo, A., R. Brown and C.L. Wrench, 1982: A field study of nocturnal stratocumulus: III. High resolution radiative and microphysical observations. *Quart. J. Roy. Meteor. Soc.*, **108**, 145-166.

Soong, S.-T. and Y.Ogura, 1980: Response of tradewind cumuli to large-scale processes. *J. Atmos. Sci.*, **37**, 2035-2050.

Squires, P., 1958: Penetrative downdraughts in cumuli. *Tellus*, **10**, 382-389.

Stackpole, J.D., 1967: Numerical analysis of atmospheric soundings. *J. Appl. Meteor.*, **6**, 464-467.

Stage, S.A. and J.A. Businger, 1981a: A model for entrainment into a cloud-topped marine boundary layer. Part I: model description and application to a cold-air outbreak episode. *J. Atmos. Sci.*, **38**, 2213-2229.

Stage, S.A. and J.A. Businger, 1981b: A model for entrainment into a cloud-topped marine boundary layer. Part II: discussion of model behavior and comparison with other models. *J. Atmos. Sci.*, **38**, 2230-2242.

Stephens, G.L., 1978: Radiation profiles in extended water clouds. II: parameterization schemes. *J. Atmos. Sci.*, **35**, 2123-2132.

Stith, J.L., D.A. Griffith, R.L. Rose, J.A. Flueck, J.R.Miller, Jr., and P.L. Smith, 1986: Aircraft observations of transport and diffusion in cumulus clouds. *J. Clim. Appl. Meteor.*, **25**, 1959-1970.

Stull, R.B., 1984: Models and measurements of the interaction between the mixed layer and fair-weather cumulus clouds: Part 2. Some preliminary measurements. *Transactions of An APCA Speciality Conference on Environmental Impact of Natural Emissions* (V.P. Aneja, Ed.), Air Pollution Control Assoc., 326-337.

Stull, R.B., 1985: A fair-weather cumulus cloud classification scheme for mixed layer studies. *J. Clim. Appl. Meteor.*, **24**, 49-56.

Stull, R.B., 1987: Applications of the transilient turbulence parameterization to atmospheric boundary-layer simulations. *Bound.-Layer Meteor.*, **40**, 209-239.

Tag, P.M. and S.W. Payne, 1987: An examination of the breakup of marine stratus: a three dimensional numerical investigation. *J. Atmos. Sci.*, **44**, 208-223.

Telford, J.W., 1985: Comments on 'Outlook for research on subtropical marine stratiform clouds'. *Bull. Amer. Meteor. Soc.*, **66**, 850-852.

Telford, J.W. and S.K. Chai, 1980: A new aspect of condensation theory. *Pure Appl. Geophys.*, **118**, 720-742.

Telford, J.W. T.S. Keck and S.K. Chai, 1984: Entrainment at cloud tops and the droplet spectra. *J. Atmos. Sci.*, **41**, 3170-3179.

Tetens, O., 1930: Über einige meteorologische Vegriffe. *Z. Geophys.*, **6**, 297-309.

Turton, J.D. and R. Brown, 1987: A comparison of a numerical model of radiation fog with detailed observations. *Quart. J. Roy. Meteor. Soc.*, **113**, 37-54.

Turton, J.D., and S. Nicholls, 1987: A study of the diurnal variation of stratocumulus using a multiple mixed layer model. *Quart. J. Roy. Meteor. Soc.*, **113**, 969-1010.

Wang, S. and B.A. Albrecht, 1986: A stratocumulus model with an internal circulation. *J. Atmos. Sci.*, **43**, 2374-2391.

Wai, M.M.-K., 1987: A numerical study of the marine stratocumulus cloud layer. *Bound.-Layer Meteor.*, **40**, 241-267.

Welch, R.M. and M.G. Ravichandran, 1985: Prediction of quasi-periodic oscillations in mature radiation fogs. *J. Atmos. Sci.*, **42**, 2888-2897.

Welch, R.M. and B.A. Wielicki, 1984: Stratocumulus cloud field reflected fluxes: the effect of cloud shape. *J. Atmos. Sci.*, **41**, 3085-3103.

Welch, R.M. and B.A. Wielicki, 1985: A radiative parameterization of stratocumulus cloud fields. *J. Atmos. Sci.*, **42**, 2888-2897.

Welch, R.M. and B.A. Wielicki, 1986: The stratocumulus nature of fog. *J. Clim. Appl. Meteor.*, **25**, 101-111.

Wexler, A., 1976: Vapor pressure formulation for water in range 0 to 100°C. A revision. *J. Res. Nat. Bur. Stand.*, **80A**, 775-785.

Wilde, N.P., R.B. Stull, and E.W. Eloranta, 1985: The LCL zone and cumulus onset. *J. Clim. Appl. Meteor.*, **24**, 640-657.

Yamada, T. and C.-Y.J.Kao, 1986: A modeling study on the fair weather marine boundary layer of the GATE. *J. Atmos. Sci.*, **43**, 3186-3199.

Yuen, C.-W., 1985: Dynamical modeling of flow in cumulus-filled boundary layers. *J. Atmos. Sci.*, **42**, 113-134.

13.8 Exercises

1) Given the following wind and θ_v profiles in a stratocumulus-topped mixed layer. Indicate in the table below the sign (+ , - , 0) of each term of the simplified turbulence kinetic energy (e) equation for each region. (The shaded region represents cloud.)

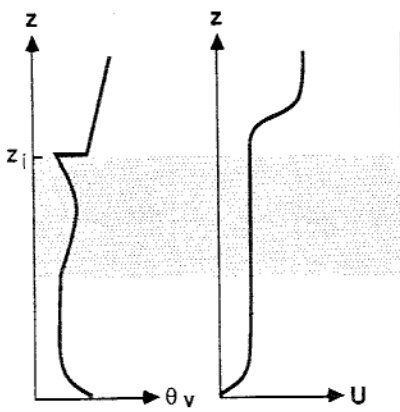

$de/dt = (g/\overline{\theta_v})\,\overline{w'\theta_v'}$	$- \overline{u'w'}\,\partial\overline{U}/\partial z$	$- \partial(\overline{w'e'})/\partial z$	$- \varepsilon$	
0				
+				
0				
0				
0				
0				

2) What is the approximate relationship between static energies and potential temperatures?

3) Given the following data points of (p, θ_L, r_T) in units of (kPa, K, g/kg) representing an environmental sounding: (100, 303, 19) (95, 303, 19) (90, 303, 19) (85, 305, 13) (80, 306, 10) (70, 312, 8) (60, 322, 5) (50, 335, 3) (40, 355, 2).

a) Plot these on a conserved-variable diagram (θ_L vs. r_T).

b) Suppose that a cloud exists in this environment, with a top at 60 kPa and base at 90 kPa. Draw the mixing line on the diagram, and plot the points corresponding to the following mixtures of environmental air from cloud top and cloud base (top,base): (50%, 50%), (30%, 70%), (20%, 80%), and (10%, 90%).

c) If there is additional mixing within the cloud (for example, the 50/50 mixture air mixing with the 10/90 mixture air), where do these mixtures fall on the mixing line?

4) Suppose the mixed layer includes the points at 100 to 90 kPa in the previous example. Where do these mixed layer points fall on the conserved variable diagram?

5) a) Given the atmospheric measurements in the table below, calculate the remaining thermodynamic variables to fill in the table. Assume that the cloud, for which data was supplied, is embedded within the given environment.

b) Plot all varieties of potential temperature as a function of height on the same graph.

c) Plot all varieties of static energies (both moist and dry) on the same graph.

d) At what pressure does neutral buoyancy (limit of convection) occur for the cloudy air specified in the table, and for a parcel rising from cloud base?

e) Calculate the CAPE in units of m^2/s^2 of the actual cloudy air, and for an air parcel rising from cloud base.

f) Assuming no entrainment, mixing, or friction, what vertical velocity would an air parcel have at the limit of convection if it started at cloud base with an upward velocity of 1 m/s? About how far above the LOC would the air parcel overshoot (i.e., where is cloud top)?

g) What processes might be responsible for the differences between actual in-cloud measurements and the idealized moist parcel ascent?

Measurements in the environment:

p (kPa)	T (°C)	r (g/kg)	r sat (g/kg)	r_L (g/kg)	Tv (°C)	θ (K)	θ_v (K)	θ_e (K)	θ_L (K)	θ_{es} (K)	s (J/g)	s_v (J/g)	s_e (J/g)	s_L (J/g)	s_{es} (J/g)
100	30	20													
90	21	15													
80	14	10													
70	9	9													
60	5	5													
50	1	3													
40	0	2													

Measurements in the cloud:

p (kPa)	T (°C)	r (g/kg)	r sat (g/kg)	r_L (g/kg)	Tv (°C)	θ (K)	θ_v (K)	θ_e (K)	θ_L (K)	θ_{es} (K)	s (J/g)	s_v (J/g)	s_e (J/g)	s_L (J/g)	s_{es} (J/g)
90	22			0.5											
80	16			2.0											
70	11			5.0											
60	7			4.0											

6) If $\overline{w's_L'} = 0.05$ (J/g)(m/s) and $\overline{w'r_T'} = 0.05$ (g/kg)(m/s), then calculate the value of the buoyancy flux, $\overline{w's_v'}$.

7) Find the saturation vapor pressure and mixing ratio for T = 20°C and P = 90 kPa.

8) Find the saturation-point temperature and pressure for P = 85 kPa, T = 20°C, r = 8 g/kg.
9) Find and plot the net solar radiation as a function of depth within a stratocumulus cloud, given z_T = 1000 m, z_B = 700 m, solar zenith angle = 70°, and K = -900 W/m^2. What are the values of the e-folding decay length, bulk cloud albedo, and bulk cloud absorption?
10) Find the change in net longwave flux across the top and bottom of a stratocumulus cloud, assuming the following temperatures: $T_{surface}$ = 30°C, $T_{cloud\ base}$ = 25°C, $T_{cloud\ top}$ = 15°C, and T_{sky} = 100 K.
11) Just above cloud top: P = 80 kPa, T = 10°C, r_T = 0.5 g/kg. Just below cloud top: P = 80 kPa, T = 5°C, r_T = 10 g/kg. Is this stratocumuls cloud unstable for cloud-top entrainment?
12) Calculate and plot the distribution of cloud diameters, assuming the lognormal location and shape parameters are 750 m and 0.75, respectively.